Pseudospectral solution of three-dimensional nonlinear sloshing in a shallow water rectangular tank

Pseudospectral solution of three-dimensional nonlinear sloshing in a shallow water rectangular tank

Ming-Jyh Chern [a,b], Nima Vaziri [c,*], Sam Syamsuri [a], Alistair G.L. Borthwick [d]

[a] Department of Mechanical Engineering, National Taiwan University of Science and Technology, 43 Sec. 4 Keelung Road, Taipei 10607, Taiwan
[b] Ecological Engineering Research Unit, National Taiwan University, No. 1 Sec. 4 Roosevelt Road, Taipei 10617, Taiwan
[c] Department of Physics, Karaj Branch, Islamic Azad University, Karaj, Iran
[d] Department of Civil and Environmental Engineering, University College Cork, Cork, Ireland

ABSTRACT

In this study, a pseudospectral σ-transformation model is developed to simulate fully nonlinear sloshing waves in a three-dimensional shallow water rectangular tank. The σ-transformation maps the physical domain including the water free surface onto a fixed rectangular computational domain. Chebyshev collocation formulae are used to discretize the governing equation and boundary conditions in the computational domain. The numerical model is validated for three well known analytical and numerical sloshing problems. An extensive study is then made of sloshing in a shallow water tank, and the effects of excitation frequency, base aspect ratio, and amplitude of excitation on the wave motions and patterns are considered. Wave regimes and patterns are considerably influenced by the base aspect ratio. In a shallow water tank with a non-square base, different wave regimes are observed during small-amplitude resonant excitation. Also, bores develop during large amplitude resonance excitation. The present study demonstrates that a pseudospectral σ-transformation can accurately model nonlinear sloshing waves in a rectangular tank. Also, results show that contrary to the situation in deeper water tanks, sloshing in shallow water strongly depends on the base aspect ratio.

© 2012 Elsevier Ltd. All rights reserved.

1. Introduction

When subject to external excitation, liquid in a container experiences sloshing motions, which can become resonant as the tank excitation frequency approaches the natural frequency of the liquid within the tank. Sloshing is of considerable importance whenever liquids are transported or stored in tanks, and so the analysis of sloshing motions is relevant to a wide range of engineering disciplines. Resonant sloshing waves can induce large loads on the container walls and associated support structures, reducing the operational fatigue life and even causing failure when the pressure is sufficiently high.

Many research studies have focused on resonant fluid sloshing. Ibrahim et al. (2001) reviewed the use (up to the year 2000) of different flow models in predicting fluid sloshing. More recently, Ibrahim (2005) and Faltinsen and Timokha (2009) have provided extensive reviews on the physics and applications of liquid sloshing. Faltinsen et al. (2005) divided the main approaches to theoretical analysis of sloshing into three categories: analytic methods for standing waves based

Nomenclature

A_i	amplitude, m $[i=x,y,z]$	u	typical smooth function
a	length of tank, m	$\hat{\mathbf{u}}$	vector of Chebyshev coefficients
b	width of tank, m	x_j	collocation points $[j=0,…,N]$
d	still water depth, m	X	σ-transformation of x
$G^{(q)}$	matrix of PSME coefficients $[q=1,2,…]$	X_{tank}	forced periodic motion in x direction, m
$\hat{\mathbf{G}}^{(q)}$	inverse of the matrix $G^{(q)}$ $[q=1,2,…]$	Y	σ-transformation of y
g	acceleration due to gravity, m/s^2	Y_{tank}	forced periodic motion in y direction, m
h	elevation of wave free surface vertically above bed of tank, m	Z_{tank}	forced periodic motion in z direction, m
L	number of collocation points in σ direction	*Greek symbols*	
M	number of collocation points in Y direction		
N	number of collocation points in X direction	η	free surface elevation above the still water level, m
q	order of derivation	σ	σ-transformation of z
$\mathbf{T}$	matrix formed of Chebyshev polynomials	Φ	transformed value of φ
$\hat{\mathbf{T}}$	inverse of matrix $\mathbf{T}$	φ	velocity potential, m^2/s
t	time, s	Ω_i	excitation frequency, rad/s $[i=x,y,z]$
Δt	time step, s	ω_{mn}	natural frequencies of rectangular tank, rad/s $[m,n=0,1,2,…]$
Δt^*	non-dimensional time step		

on low-order asymptotic expansions (see e.g. Abramson 1966; Hutton, 1962; Moiseyev, 1958; Penny and Price, 1952), computational fluid dynamics (CFD), and multimodal or pseudospectral methods. Whereas analytical solutions are available for low-amplitude sloshing in simple container geometries, such analysis does not readily extend to large-amplitude sloshing in complicated geometries (see e.g. El-Sayad et al., 1999). Instead numerical models are widely applied to the study of nonlinear free surface motions of liquids undergoing sloshing in tanks. Examples include Faltinsen (1978), Okamoto and Kawahara (1990), Chen et al. (1996), Armenio and La Rocca (1996), Chern et al. (1999), Frandsen (2004) and Sun et al. (2010) who used various numerical methods to simulate two-dimensional sloshing problems.

It is debatable whether two-dimensional sloshing theory should be used to predict three-dimensional sloshing. Faltinsen et al. (2003) observed that resonant excitation at the lowest natural frequency could lead to two-dimensional motions becoming unstable, then highly three-dimensional, even chaotic. Faltinsen et al. (2003, 2005, 2006) conducted a series of studies into three-dimensional sloshing, including resonant nonlinear sloshing in square and nearly square basins. A whole variety of different numerical schemes have been used to predict sloshing. Huang and Hsiung (1996) solved the depth-averaged shallow water equations in simulating green water sloshing on the deck of a ship. Wu et al. (1998) developed a finite element potential flow solver to simulate three-dimensional nonlinear wave sloshing in a tank. Akyildiz and Erdem Unal (1996) used a volume of fluid (VOF) technique to model three-dimensional sloshing in a rectangular tank. Wu and Chen (2009) developed a time-independent finite difference method to predict three-dimensional wave sloshing in a tank. Curadelli et al. (2010) used the finite element method and study resonant frequencies in an elevated spherical container. Alemi Ardakani and Bridges (2011) derived a new set of shallow water equations and simulated sloshing in three dimensions.

Fully nonlinear, time-domain potential flow solvers based on high order methods, such as spectral elements are particularly well suited to the study of large amplitude waves in shallow water. Hussaini and Zang (1987) provides a detailed review of spectral elements applications in computational fluid dynamics. The present study employs the Chebyshev pseudospectral matrix-element (PSME) method (Ku and Hatziavramidis, 1985) to model the three-dimensional free surface sloshing motions of an inviscid fluid. Fully nonlinear potential theory is used to describe mathematically the problem, which is mapped from the physical domain onto a σ-transformed rectangular coordinate system. The present model is an extension of a 2D nonlinear sloshing model by Chern et al. (1999). A similar approach was also used by Chern et al. (2001) to simulate fully nonlinear free surface motions in a cylindrical domain. It should be noted that the σ-transformation involves a unique mapping between the tank bed and liquid free surface, and so is not applicable to overturning or breaking waves. The aim of the present work is the study of the capability of the PSME method as a high order numerical method on 3-D sloshing. Results are presented for three-dimensional sloshing of shallow water in a rectangular tank for a ratio of water depth to tank length, $d/a=0.1$.

2. Mathematical model of free surface waves in the Cartesian domain

Fig. 1 shows an illustration of the model tank of length a and width b, with still water depth d. In the numerical cases considered herein, six reference points are selected: the four free surface corner vertices (Points A, B, C and D) and the free surface mid points along the tank in the ox and oy axes (Points E and F, respectively). Assuming that the fluid inside the
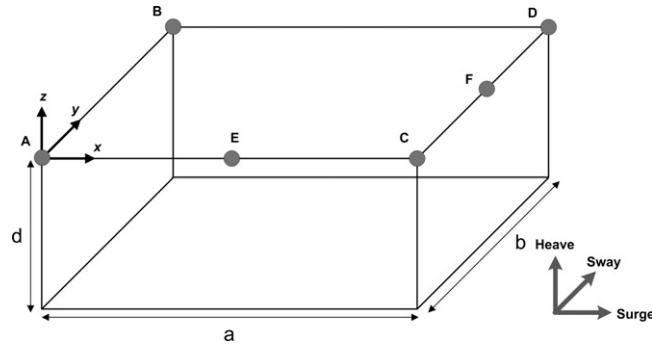
Fig. 1. Schematic view of the tank (with the length of a, the width of b and the still water depth of d) and the excitation directions.

tank is incompressible, inviscid, and irrotational, the governing equation is

$$\frac{\partial^2 \varphi}{\partial x^2} + \frac{\partial^2 \varphi}{\partial y^2} + \frac{\partial^2 \varphi}{\partial z^2} = 0, \tag{1}$$

where φ is the velocity potential. At the solid lateral wall and bed boundaries, the velocity components are set to zero, such that

$$\frac{\partial \varphi}{\partial x} = 0 \quad at \ x = 0 \ \text{and} \ x = a, \tag{2}$$

$$\frac{\partial \varphi}{\partial y} = 0 \quad at \ y = 0 \ \text{and} \ y = b, \tag{3}$$

and

$$\frac{\partial \varphi}{\partial z} = 0 \quad at \ z = -d. \tag{4}$$

Consider a tank undergoing forced periodic motion defined by

$$X_{\text{tank}} = A_x \sin(\Omega_x t),$$
$$Y_{\text{tank}} = A_y \sin(\Omega_y t),$$
$$Z_{\text{tank}} = A_z \sin(\Omega_z t), \tag{5}$$

where A is the amplitude of the displacement, t is time, and Ω is the excitation frequency. These excitations correspond to surge, sway and heave, respectively. It is relevant to note that, based on the linear solution for sloshing in a tank (see e.g., Faltinsen, 1978; Wu et al., 1998), the natural frequencies of sloshing in a rectangular tank, ω_{mn} are

$$\omega_{mn}^2 = g\pi \sqrt{\left(\frac{m^2}{a^2} + \frac{n^2}{b^2}\right)} \tanh\left(\pi \sqrt{\left(\frac{m^2}{a^2} + \frac{n^2}{b^2}\right)} d\right) \quad (m,n = 0,1,2,\ldots). \tag{6}$$

The first natural frequency in the x direction (ω_{10}) is obtained by taking $m=1$ and $n=0$. Similarly the first natural frequency in the y direction (ω_{01}) is obtained by taking $m=0$ and $n=1$. The value of Ω is proportional to ω_{mn}. For example the tank can become resonant in the x direction when Ω_x approaches ω_{10} (e.g. $\Omega_x = 0.9999\omega_{10}$).

At the gas–liquid interface, the nonlinear dynamic and kinematic free surface boundary conditions are

$$\frac{\partial \varphi}{\partial t} = -g\eta - \frac{1}{2}\left[\left(\frac{\partial \varphi}{\partial x}\right)^2 + \left(\frac{\partial \varphi}{\partial y}\right)^2 + \left(\frac{\partial \varphi}{\partial z}\right)^2\right] - x\frac{d^2 X_{\text{tank}}}{dt^2} - y\frac{d^2 Y_{\text{tank}}}{dt^2} - z\frac{d^2 Z_{\text{tank}}}{dt^2} \quad at \ z = \eta \tag{7}$$

and

$$\frac{\partial \eta}{\partial t} = \frac{\partial \varphi}{\partial z} - \frac{\partial \varphi}{\partial x}\frac{\partial \eta}{\partial x} - \frac{\partial \varphi}{\partial y}\frac{\partial \eta}{\partial y} \quad at \ z = \eta, \tag{8}$$

where η is the free surface elevation above the still water level and g is the acceleration due to gravity. The tank motion acceleration components, $d^2 X_{\text{tank}}/dt^2$, $d^2 Y_{\text{tank}}/dt^2$ and $d^2 Z_{\text{tank}}/dt^2$, are obtained by twice differentiating Eq. (5). It should be noted that this study is focused on the surge and the sway excitations only. Therefore the last term of Eq. (5) (and the transformed form of it) can be omitted. Initial conditions for the velocity potential and free surface elevation are given by

$$\varphi(x,y,z,0) = -x\frac{dX_{\text{tank}}}{dt}\bigg|_{t=0} - y\frac{dY_{\text{tank}}}{dt}\bigg|_{t=0}, \tag{9}$$

and

$$\eta(x,y,0) = 0. \tag{10}$$

2.1. σ-Transformation

The σ-transformation involves mapping the physical domain $x,y,z \in [0,a] \times [0,b] \times [-d,\eta]$ onto the rectangular region $X,Y,\sigma \in [-1,1] \times [-1,1] \times [-1,1]$. The transformation equations are

$$X = -1 + \frac{2x}{a},$$
$$Y = -1 + \frac{2y}{b},$$
$$\sigma = -1 + \frac{2(z+d)}{h}, \tag{11}$$

where

$$h = \eta + d. \tag{12}$$

A consequence of this transformation is that the free surface is fixed in the computational domain at $Y=1$, and so cannot model overturning waves or roof impacts. Applying the above transformation, the velocity potential $\varphi(x,y,z,t)$ in the physical domain is mapped onto $\Phi(X,Y,\sigma,t)$. Invoking the chain rule and rearranging, the transformed governing equation becomes

$$
\left(\frac{2}{a}\right)^2 \frac{\partial^2 \Phi}{\partial X^2} + \left(\frac{2}{b}\right)^2 \frac{\partial^2 \Phi}{\partial Y^2}
$$
$$
+ \left[\left(\frac{2}{a}\right)^2 \left(\frac{2\sigma}{h^2}\right)\left(\frac{\partial \eta}{\partial X}\right)^2 - \left(\frac{2}{a}\right)^2 \left(\frac{\sigma}{h}\right)\left(\frac{\partial^2 \eta}{\partial X^2}\right) + \left(\frac{2}{b}\right)^2 \left(\frac{2\sigma}{h^2}\right)\left(\frac{\partial \eta}{\partial Y}\right)^2 - \left(\frac{2}{b}\right)^2 \left(\frac{\sigma}{h}\right)\left(\frac{\partial^2 \eta}{\partial Y^2}\right)\right] \frac{\partial \Phi}{\partial \sigma}
$$
$$
- \left[\left(\frac{2}{a}\right)^2 \left(\frac{2\sigma}{h}\right)\left(\frac{\partial \eta}{\partial X}\right)\right] \frac{\partial^2 \Phi}{\partial X \partial \sigma} - \left[\left(\frac{2}{b}\right)^2 \left(\frac{2\sigma}{h}\right)\left(\frac{\partial \eta}{\partial Y}\right)\right] \frac{\partial^2 \Phi}{\partial Y \partial \sigma}
$$
$$
+ \left[\left(\frac{2}{a}\right)^2 \left(\frac{\sigma^2}{h^2}\right)\left(\frac{\partial \eta}{\partial X}\right)^2 + \left(\frac{2}{b}\right)^2 \left(\frac{\sigma^2}{h^2}\right)\left(\frac{\partial \eta}{\partial Y}\right)^2 + \left(\frac{1}{h^2}\right)\right] \frac{\partial^2 \Phi}{\partial \sigma^2} = 0. \tag{13}
$$

The transformed dynamic and kinematic free surface boundary conditions are

$$
\frac{\partial \Phi}{\partial t} = \left(\frac{\sigma}{h}\right)\left(\frac{\partial \eta}{\partial t}\right)\left(\frac{\partial \Phi}{\partial \sigma}\right) - g\eta
$$
$$
- \frac{1}{2}\left[\left[\left(\frac{2}{a}\right)\left(\frac{\partial \Phi}{\partial X}\right) - \left(\frac{2}{a}\right)\left(\frac{\sigma}{h}\right)\left(\frac{\partial \eta}{\partial X}\right)\left(\frac{\partial \Phi}{\partial \sigma}\right)\right]^2 + \left[\left(\frac{2}{b}\right)\left(\frac{\partial \Phi}{\partial Y}\right) - \left(\frac{2}{b}\right)\left(\frac{\sigma}{h}\right)\left(\frac{\partial \eta}{\partial Y}\right)\left(\frac{\partial \Phi}{\partial \sigma}\right)\right]^2\right.
$$
$$
\left. + \left[\left(\frac{1}{h}\right)\left(\frac{\partial \Phi}{\partial \sigma}\right)\right]^2\right] - \left(\frac{aX}{2}\right)\frac{d^2 X_{\text{tank}}}{dt^2} - \left(\frac{bY}{2}\right)\frac{d^2 Y_{\text{tank}}}{dt^2} - \eta\frac{d^2 Z_{\text{tank}}}{dt^2} \quad \text{at } \sigma = 1 \tag{14}
$$

and

$$
\frac{\partial \eta}{\partial t} = \left(\frac{1}{h}\right) + \left[\left(\frac{2}{a}\right)\left(\frac{\sigma}{h}\right)\left(\frac{\partial \eta}{\partial X}\right) + \left(\frac{2}{b}\right)\left(\frac{\sigma}{h}\right)\left(\frac{\partial \eta}{\partial Y}\right)\right] \frac{\partial \Phi}{\partial \sigma}
$$
$$
- \left(\frac{2}{a}\right)^2 \left(\frac{\partial \eta}{\partial X}\right)\frac{\partial \Phi}{\partial X} - \left(\frac{2}{b}\right)^2 \left(\frac{\partial \eta}{\partial Y}\right)\frac{\partial \Phi}{\partial Y} \quad \text{at } \sigma = 1. \tag{15}
$$

The transformed bed condition is

$$\frac{\partial \Phi}{\partial \sigma} = 0 \quad \text{at } \sigma = -1. \tag{16}$$

The transformed lateral wall boundary conditions are

$$\frac{\partial \Phi}{\partial X} - \left(\frac{\sigma}{h}\right)\left(\frac{\partial \eta}{\partial X}\right)\frac{\partial \Phi}{\partial \sigma} = 0 \quad \text{at } X = -1 \text{ and } X = 1 \tag{17}$$

and

$$\frac{\partial \Phi}{\partial Y} - \left(\frac{\sigma}{h}\right)\left(\frac{\partial \eta}{\partial Y}\right)\frac{\partial \Phi}{\partial \sigma} = 0 \quad \text{at } Y = -1 \text{ and } Y = 1. \tag{18}$$

3. Pseudospectral matrix-element method

The Chebyshev expansion of $u(x)$, a smooth function on $x \in [-1,1]$, is

$$\mathbf{u} = T\hat{\mathbf{u}}, \tag{19}$$

where $\mathbf{T}$ is a Chebyshev polynomial matrix and $\hat{\mathbf{u}}$ is a vector of Chebyshev coefficients. Collocation points in the interval $[-1, 1]$ are located at

$$x_j = \cos\left(\frac{j\pi}{N}\right), \quad j = 0,1,2,\dots,N, \tag{20}$$

with corresponding discrete values of the function,

$$u_j = u(x_j) \quad \text{and} \quad T_{jk} = T_k(x_j). \tag{21}$$

Transforming from physical space to Chebyshev spectral space,

$$\hat{u}_k = \frac{2}{NC_k} \sum_{j=0}^{N} \frac{1}{C_j} u(x_j) \cos\frac{\pi kj}{N}, \quad k = 0,1,\dots,N, \tag{22}$$

where

$$C_j, C_k = \begin{cases} 2, & j, k = 0, N, \\ 1, & 1 \leq j, k \leq N-1. \end{cases} \tag{23}$$

Writing this in matrix notation,

$$\hat{\mathbf{u}} = \hat{\mathbf{T}}u, \tag{24}$$

where $\hat{\mathbf{T}}$ is the inverse of $\mathbf{T}$, with each entry defined as

$$\hat{T}_{kj} = \frac{2}{NC_kC_j} \cos\frac{\pi kj}{N}. \tag{25}$$

In Chebyshev spectral space, the qth derivative of the function u is written as

$$\frac{d^q u_j}{dx^q} = \sum_{k=0}^{N} \hat{u}_k^{(q)} T_k(x_j), \tag{26}$$

in which $\hat{u}_k^{(q)}$ are the coefficients of the derivative expansion. Again, in matrix notation, we have

$$\hat{\mathbf{u}}^{(q)} = \mathbf{G}^{(q)}\hat{\mathbf{u}}. \tag{27}$$

In practice, Eq. (26) is simplified to give

$$\frac{d^{(q)}\mathbf{u}}{dx^{(q)}} = \hat{\mathbf{G}}^{(q)}\mathbf{u}, \tag{28}$$

in which

$$\hat{\mathbf{G}}^{(q)} = \mathbf{T}\mathbf{G}^{(q)}\hat{\mathbf{T}}, \tag{29}$$

where

$$\mathbf{G}^{(q)} = (\mathbf{G}^{(1)})^{\mathbf{q}}, \tag{30}$$

with the matrix elements given by

$$G_{ij}^{(1)} = \begin{cases} 0 & \text{if } i \geq j \text{ or } i+j \text{ even}, \\ \frac{2j}{C_i} & \text{otherwise.} \end{cases} \tag{31}$$

$C_i = 1$ everywhere, except at the end points where $C_i = 2$. In the PSME method, Eq. (28) is used to determine the spectral derivatives. If $\mathbf{q} = 1$, then $\hat{\mathbf{G}}^{(q)}$ is the first derivative, and so on.

4. PSME modelling

Next, the transformed domain is discretized according to the Chebyshev collocation formula given by Eq. (20). Let N, M and L be the total numbers of collocation points in the X, Y and σ directions. Fig. 2 shows a typical σ-transformed mesh. After PSME discretization, Eq. (13) becomes

$$\left(\frac{2}{a}\right)^2 \sum_{m=0}^{N} \hat{G}X_{im}^{(2)}\Phi_{mjk} + \left(\frac{2}{b}\right)^2 \sum_{m=0}^{M} \hat{G}Y_{jm}^{(2)}\Phi_{imk} + \left[\left(\frac{2}{a}\right)^2 \left(\frac{2(Z_k+1)}{h_{ij}^2}\right)\left(\frac{\partial\eta}{\partial X}\right)_{ij}^2 - \left(\frac{2}{a}\right)^2 \left(\frac{(Z_k+1)}{h_{ij}}\right)\left(\frac{\partial^2\eta}{\partial X^2}\right)_{ij}$$
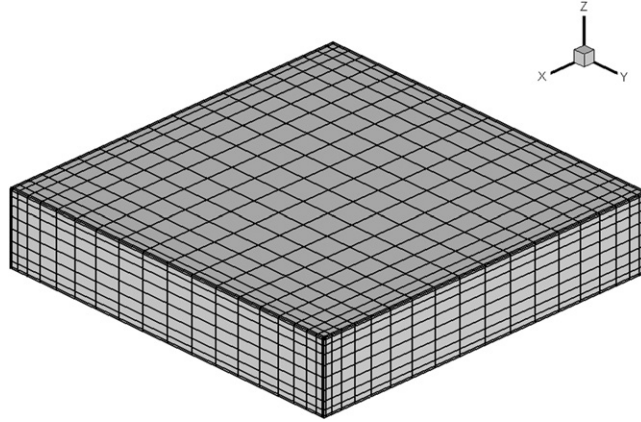
Fig. 2. A three-dimensional pseudospectral σ-transformed mesh.

$$+\left(\frac{2}{b}\right)^2\left(\frac{2(Z_k+1)}{h_{ij}^2}\right)\left(\frac{\partial\eta}{\partial Y}\right)_{ij}^2-\left(\frac{2}{b}\right)^2\left(\frac{(Z_k+1)}{h_{ij}}\right)\left(\frac{\partial^2\eta}{\partial Y^2}\right)_{ij}\Bigg]\sum_{m=0}^{L}\hat{G}\sigma_{km}^{(1)}\Phi_{ijm}$$

$$-\left[\left(\frac{2}{a}\right)^2\left(\frac{2(Z_k+1)}{h_{ij}}\right)\left(\frac{\partial\eta}{\partial X}\right)_{ij}\right]\sum_{n=0}^{N}\sum_{m=0}^{L}\hat{G}X_{in}^{(1)}\hat{G}\sigma_{km}^{(1)}\Phi_{njm}$$

$$-\left[\left(\frac{2}{b}\right)^2\left(\frac{2(Z_k+1)}{h_{ij}}\right)\left(\frac{\partial\eta}{\partial Y}\right)_{ij}\right]\sum_{n=0}^{M}\sum_{m=0}^{L}\hat{G}Y_{jm}^{(1)}\hat{G}\sigma_{km}^{(1)}\Phi_{inm}$$

$$+\left[\left(\frac{2}{a}\right)^2\left(\frac{(Z_k+1)^2}{h_{ij}^2}\right)\left(\frac{\partial\eta}{\partial X}\right)_{ij}^2+\left(\frac{2}{b}\right)^2\left(\frac{(Z_k+1)^2}{h_{ij}^2}\right)\left(\frac{\partial\eta}{\partial Y}\right)_{ij}^2+\left(\frac{1}{(Z_k+1)^2}\right)\right]\sum_{m=0}^{L}\hat{G}\sigma_{km}^{(2)}\Phi_{ijm}=0. \tag{32}$$

The discretized versions of the σ-transformed dynamic and kinematic free surface boundary conditions are

$$\frac{\partial\Phi}{\partial t}=\left(\frac{(Z_k+1)}{h_{ij}}\right)\left(\frac{\partial\eta}{\partial t}\right)_{ij}\sum_{m=0}^{L}\hat{G}\sigma_{km}^{(1)}\Phi_{ijm}-g\eta_{ij}$$

$$-\frac{1}{2}\Bigg[\left[\left(\frac{2}{a}\right)\sum_{m=0}^{N}\hat{G}X_{im}^{(1)}\Phi_{mjk}-\left(\frac{2}{a}\right)\left(\frac{(Z_k+1)}{h_{ij}}\right)\left(\frac{\partial\eta}{\partial X}\right)_{ij}\sum_{m=0}^{L}\hat{G}\sigma_{km}^{(1)}\Phi_{ijm}\right]^2$$

$$+\left[\left(\frac{2}{b}\right)\sum_{m=0}^{M}\hat{G}Y_{jm}^{(1)}\Phi_{imk}-\left(\frac{2}{b}\right)\left(\frac{(Z_k+1)}{h_{ij}}\right)\left(\frac{\partial\eta}{\partial Y}\right)_{ij}\sum_{m=0}^{L}\hat{G}\sigma_{km}^{(1)}\Phi_{ijm}\right]^2$$

$$+\left[\left(\frac{1}{h_{ij}}\right)\sum_{m=0}^{L}\hat{G}\sigma_{km}^{(1)}\Phi_{ijm}\right]^2\Bigg]-\left(\frac{aX}{2}\right)\frac{\mathrm{d}^2X_{\text{tank}}}{\mathrm{d}t^2}-\left(\frac{bY}{2}\right)\frac{\mathrm{d}^2Y_{\text{tank}}}{\mathrm{d}t^2}-\eta_{ij}\frac{\mathrm{d}^2Z_{\text{tank}}}{\mathrm{d}t^2} \tag{33}$$

and

$$\frac{\partial\eta}{\partial t}=\left(\frac{1}{h_{ij}}\right)+\left[\left(\frac{2}{a}\right)\left(\frac{(Z_k+1)}{h_{ij}}\right)\left(\frac{\partial\eta}{\partial X}\right)_{ij}+\left(\frac{2}{b}\right)\left(\frac{(Z_k+1)}{h_{ij}}\right)\left(\frac{\partial\eta}{\partial Y}\right)_{ij}\right]\sum_{m=0}^{L}\hat{G}\sigma_{km}^{(1)}\Phi_{ijm}$$

$$-\left(\frac{2}{a}\right)^2\left(\frac{\partial\eta}{\partial X}\right)_{ij}\sum_{m=0}^{N}\hat{G}X_{im}^{(1)}\Phi_{mjk}-\left(\frac{2}{b}\right)^2\left(\frac{\partial\eta}{\partial Y}\right)_{ij}\sum_{m=0}^{M}\hat{G}Y_{jm}^{(1)}\Phi_{imk}. \tag{34}$$

All time integrations are undertaken using a third order Adam-Bashforth (AB3) scheme. The discretized bottom boundary condition is

$$\sum_{m=0}^{L}\hat{G}\sigma_{km}^{(1)}\Phi_{ijm}=0. \tag{35}$$

Also, the discretized lateral wall boundary conditions are

$$\sum_{m=0}^{N}\hat{G}X_{im}^{(1)}\Phi_{mjk}-\left(\frac{(Z_k+1)}{h_{ij}}\right)\left(\frac{\partial\eta}{\partial X}\right)_{ij}\sum_{m=0}^{L}\hat{G}\sigma_{km}^{(1)}\Phi_{ijm}=0, \tag{36}$$

$$\sum_{m=0}^{M}\hat{G}Y_{jm}^{(1)}\Phi_{imk}-\left(\frac{(Z_k+1)}{h_{ij}}\right)\left(\frac{\partial\eta}{\partial Y}\right)_{ij}\sum_{m=0}^{L}\hat{G}\sigma_{km}^{(1)}\Phi_{ijm}=0 . \tag{37}$$

Starting from a prescribed initial wave form, the solution procedure is as follows: (i) calculate free surface boundary values of Φ using Eq. (33); (ii) solve the discrete governing Eq. (32) together with the bed and wall boundary conditions (35)–(37) by an iterative matrix solver; (iii) update the surface elevation, η, using Eq. (34) and (iv) move forward one time step and return to (i). In this study, Successive Over-Relaxation (SOR) was used as the iterative matrix solver.

5. Model validation

First, we consider two two-dimensional cases previously investigated by Faltinsen (1978), Wu et al. (1998) and Chern et al. (1999). The displacement of the tank takes place solely in the x-direction, such that $X_{tank} = A_x \sin(\Omega_x t)$. Initial conditions are given by Eqs. (9) and (10). The tank dimensions are $d/a = 0.5$ and $d/b = 5.0$. A linear analytical solution for this problem is given by Faltinsen (1978). The first case has non-dimensional forcing frequency $\Omega_x/\omega_{10} = 0.999$ and non-dimensional amplitude $A_x/d = 0.001$. Fig. 3 shows the numerical results and the linear analytical solution at the left hand
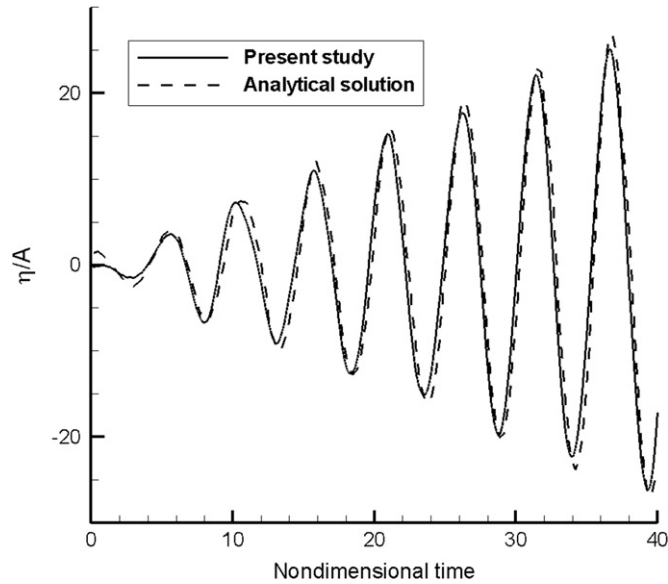

Fig. 3. Non-dimensional free surface elevation time history at Point A, for $\Omega/\omega_{10} = 0.999$.
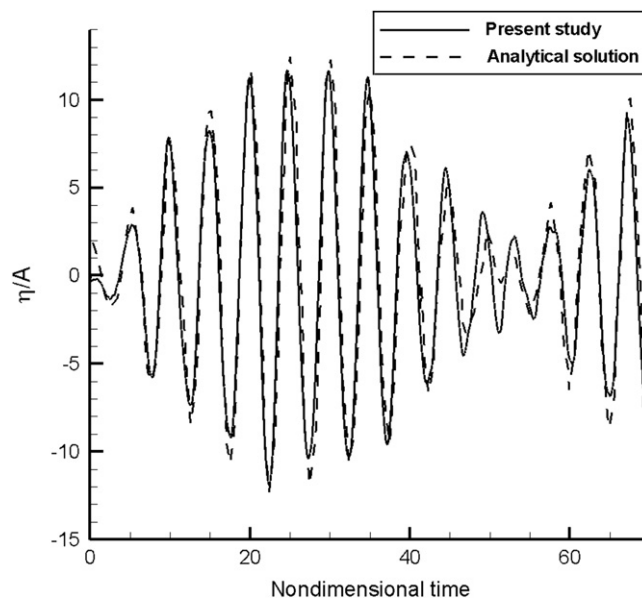

Fig. 4. Non-dimensional free surface elevation time history at Point A, for $\Omega/\omega_{10} = 1.1$.

tank wall (Point A in Fig. 1). Fig. 4 shows the corresponding results for $\Omega_x/\omega_{10}=1.1$. In both cases, the numerical predictions are in satisfactory agreement with the linear analytical solution.

Next, a three-dimensional case is examined, where the tank dimensions are $d/a=0.25$ and $d/b=0.25$. The non-dimensional excitation frequencies in the x- and y-direction are $\Omega_x/\omega_{10}=0.9999$ and $\Omega_y/\omega_{01}=0.9999$, and are applied simultaneously to the tank. No excitation is applied in the z-direction. The non-dimensional amplitudes in both directions are $A_x/d=A_y/d=0.372 \times 10^{-3}$. Fig. 5 shows the predicted wave elevation time histories of the free surface at the four corners of the tank (i.e. at Points A, B, C and D). The predictions match alternative numerical results obtained by Wu et al. (1998) who used a finite element potential flow solver. It should be noted that the present model predicts small ripples at
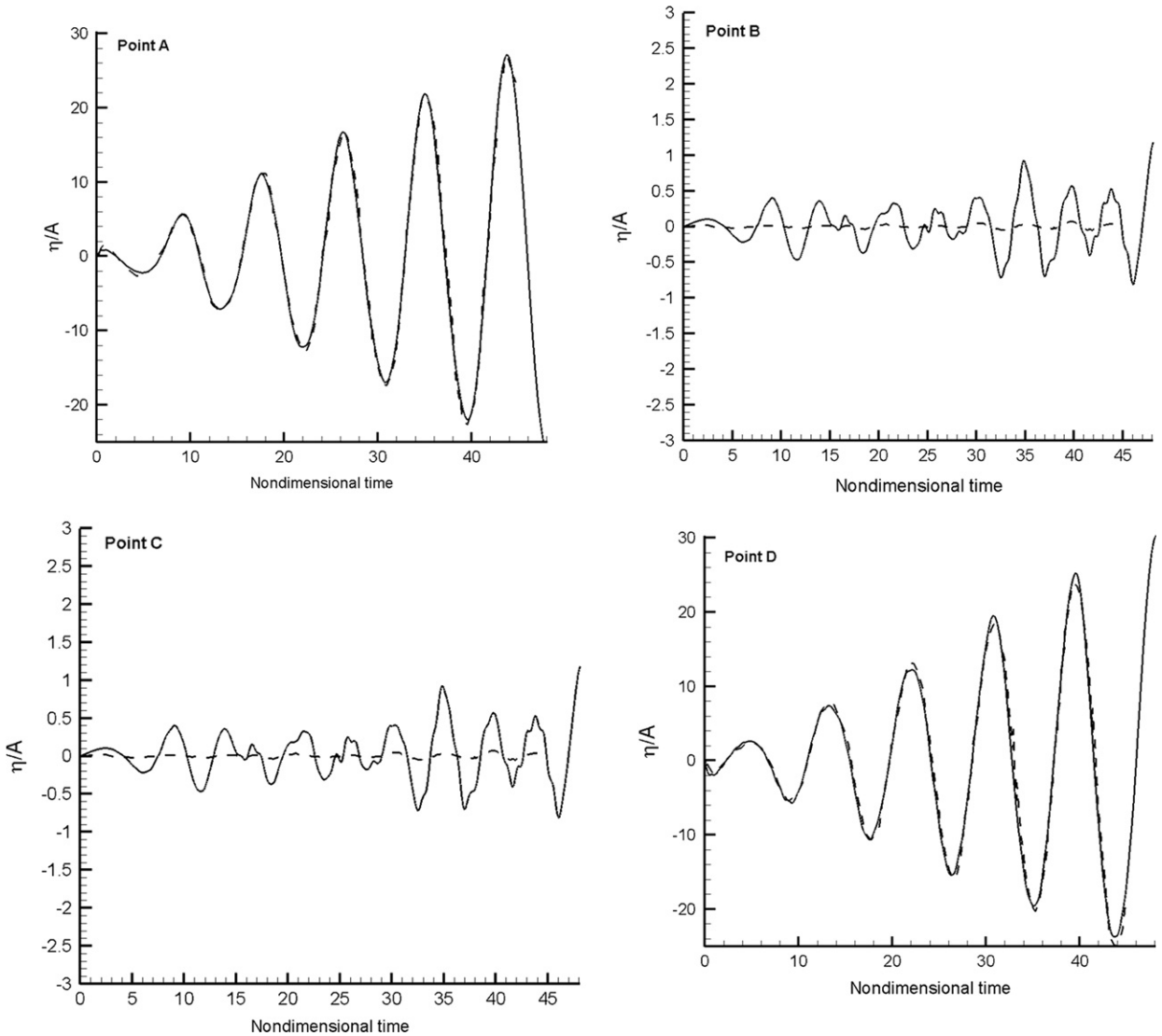

Fig. 5. Non-dimensional free surface elevation time histories at the four corners of the tank, for $\Omega_x/\omega_{10}=0.9999$ and $\Omega_y/\omega_{01}=0.9999$; — present study, – – Wu et al. (1998) model.

Table 1
Cases for collocation point and time step independency parameter study:.

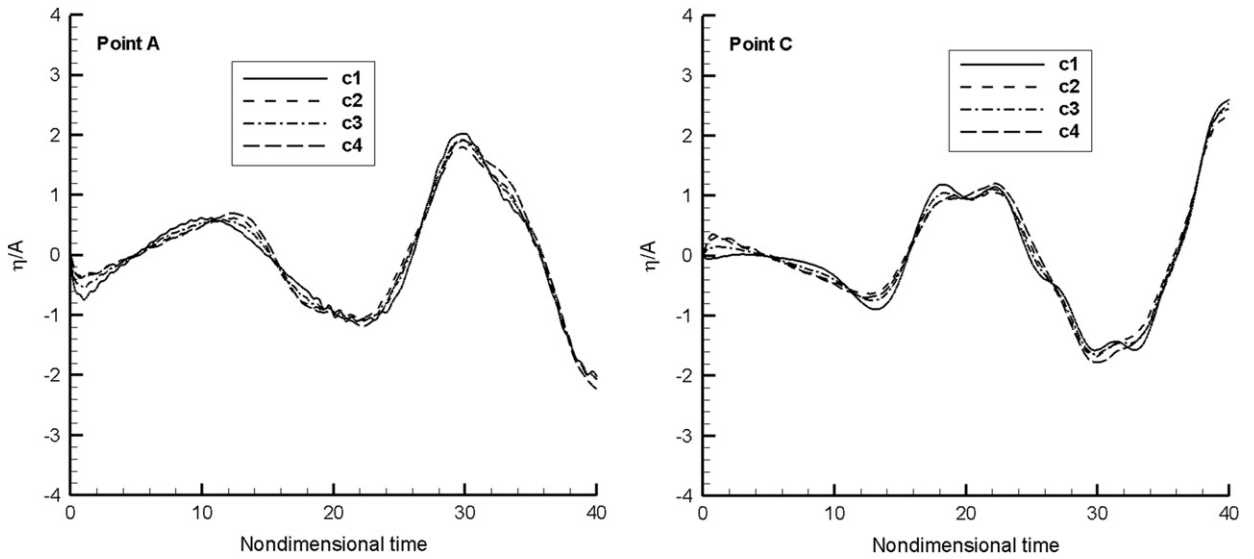| Case	N	M	L	Δt^*
c1	100	10	10	0.01
c2	100	10	10	0.001
c3	100	10	10	0.005
c4	50	5	5	0.005

Fig. 6. Comparison of water free surface elevation time histories at Points A and C for different numbers of collocation points and values of time increment.
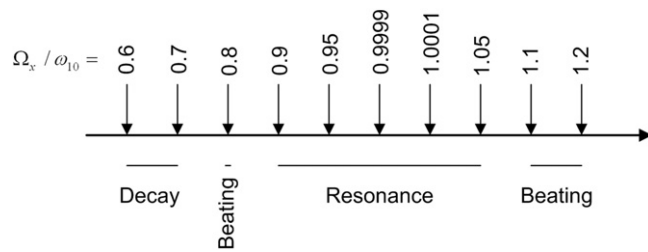

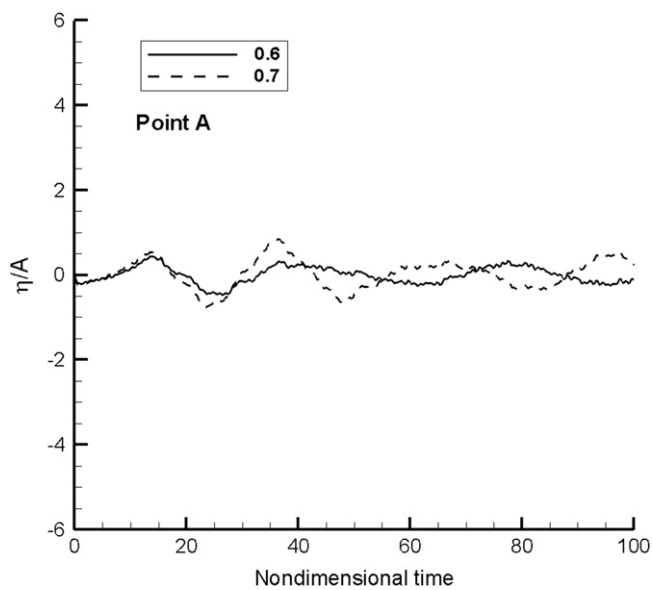**Fig. 7.** Wave pattern classification for surge excitation, $A_x/d=0.001$, $d/a=0.1$.

Fig. 8. Decay patterns for surge excitation, $A_x/d=0.001$, $d/a=0.1$, $\Omega_x/\omega_{10}=0.6\,\&\,0.7$.

Points B and C, unlike Wu et al.'s model, because of the high order nature of the spectral element scheme. In this case, we used $40 \times 40 \times 10$ collocation points in the x-, y- and z-direction, respectively, and a non-dimensional time step, $\Delta t^* = \Delta t \sqrt{(g/d)} = 0.01$. The simulation was performed on a workstation with two 3.40 GHz CPU and 3 GB RAM, and required less than 4 h CPU time to compute results up to a non-dimensional time of 50.

Table 1 lists the parameters used to test for mesh convergence (numbers of collocation points) and stability (time step). In this case, $d/a = 0.1$ and $d/b = 1$. The non-dimensional forcing frequency acts solely in the x-direction, and is $\Omega_x/\omega_{10} = 0.9999$; the non-dimensional amplitude is $A_x/d = 0.01$. Fig. 6 presents time histories of the free surface elevation at Points A and C for all the mesh convergence test cases listed in Table 1. The results show that in spite of the nonlinearity of the very steep wave considered, the spectral method gives convergent and stable results for $N = 50$, $M = 5$, $L = 5$, $\Delta t^* = 0.005$.

6. Sloshing in a tank with shallow water

The validated spectral element model is now applied to simulate sloshing in a shallow water tank. It should be noted that various criteria have been suggested in the literature for the shallow water approximation, such as $d/a \leq 0.2$ (Stoker, 1957) and
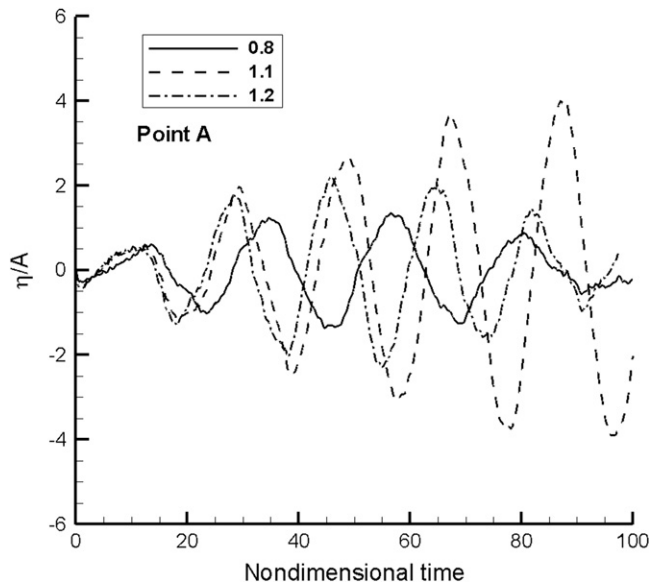

Fig. 9. Beating patterns for surge excitation, $A_x/d = 0.001$, $d/a = 0.1$, $\Omega_x/\omega_{10} = 0.8$, 1.1 and 1.2.
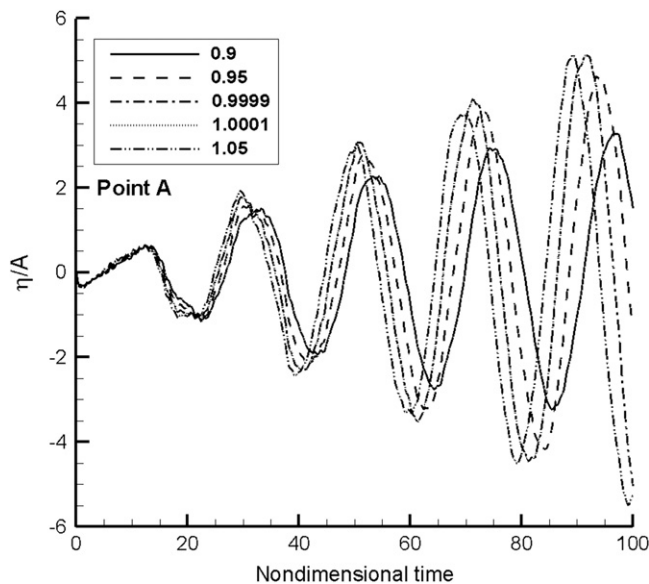

Fig. 10. Resonance patterns for surge excitation, $A_x/d = 0.001$, $d/a = 0.1$, $\Omega_x/\omega_{10} = 0.9$, 0.95, 0.9999, 1.0001 and 1.05.

$d/a \leq 0.15$ (Armenio and La Rocca, 1996). By considering series expansions, Faltinsen and Timokha (2001) propose that $d/a=0.1$ should be the border between intermediate water depth and shallow water depth. There are some papers and reports in this area (e.g. Armenio and La Rocca 1996; Faltinsen and Timokha 2001). To the authors' knowledge, there is not any comprehensive study on sloshing in three-dimensional shallow water tanks with a higher order method. Herein, we present results from a numerical parameter study on the effects of excitation frequency, base aspect ratio, and perturbation amplitude on sloshing in a shallow water rectangular tank. The dimensions of the reference tank are $d/a=0.1$ and $d/b=0.1$.

The study by Faltinsen et al. (2005) using an asymptotic modal system indicated that four different regimes of wave motion can occur in a square basin: (i) steady-state 'planar', two dimensional Stokes waves, (ii) steady-state 'diagonal'-like standing waves, which consist of oscillations from one corner of the basin to the opposite corner with much less motion in the vicinity of the other corners, (iii) steady-state 'swirling', where an almost flat crest travels around each of the four sides of the tank along with an almost flat trough propagating along on the opposite side of the tank, and (iv) 'chaotic', or irregular waves. The first three regimes in the study by Faltinsen et al. (2005) are evident in the results obtained in the present study, and discussed in the following sections.
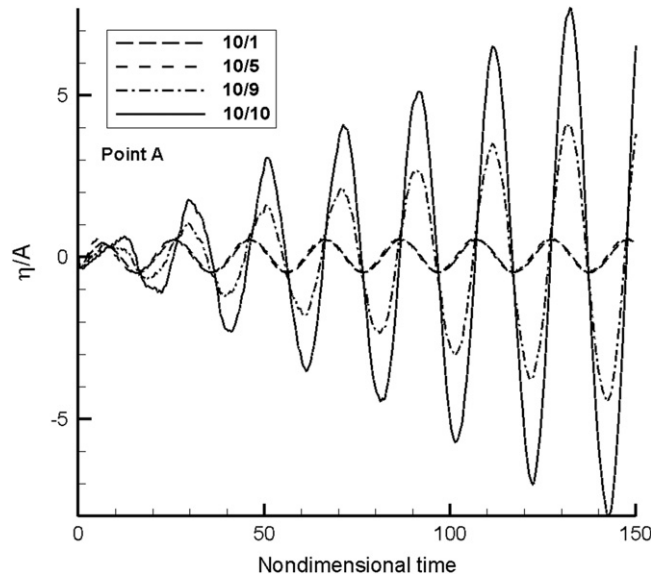

Fig. 11. Wave elevation time histories for different base aspect ratios: longitudinal excitation, $A_x/d=0.001$, $\Omega_x/\omega_{10}=0.9999$.
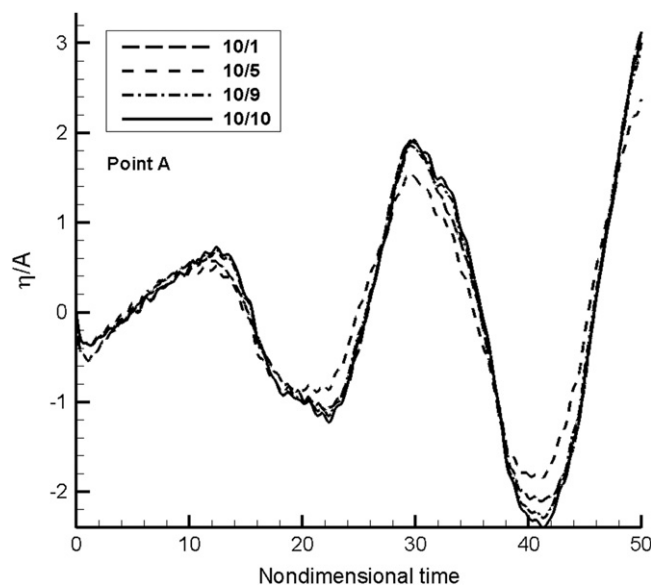

Fig. 12. Wave elevation time histories for different base aspect ratios: longitudinal excitation, $A_x/d=0.01$, $\Omega_x/\omega_{10}=0.9999$.

6.1. Effect of excitation frequency

We first consider the effect of altering the tank excitation frequency in the longitudinal direction (along the ox-axis), for 10 values chosen near to resonance in the range $0.6 \leq \Omega_x/\omega_{10} \leq 1.2$. The non-dimensional tank longitudinal excitation
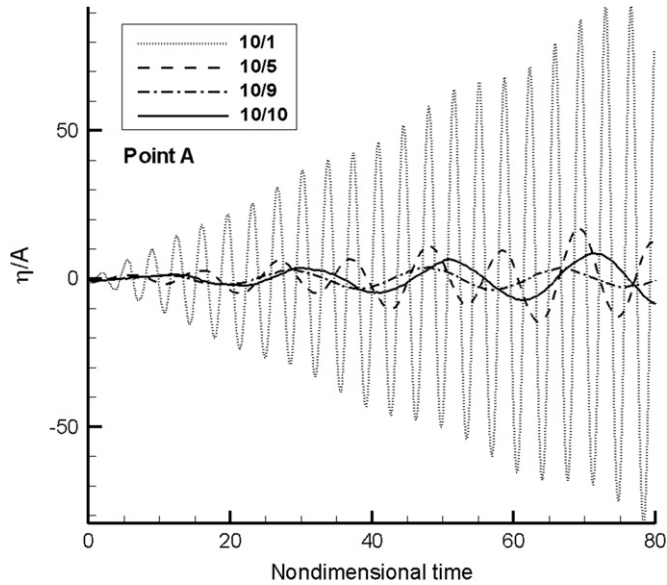

Fig. 13. Wave elevation time histories for different base aspect ratios: diagonal excitation, $A_x/d = A_y/d = 0.001$, $\Omega_x/\omega_{10} = 0.9999$, $\Omega_y/\omega_{01} = 0.9999$.
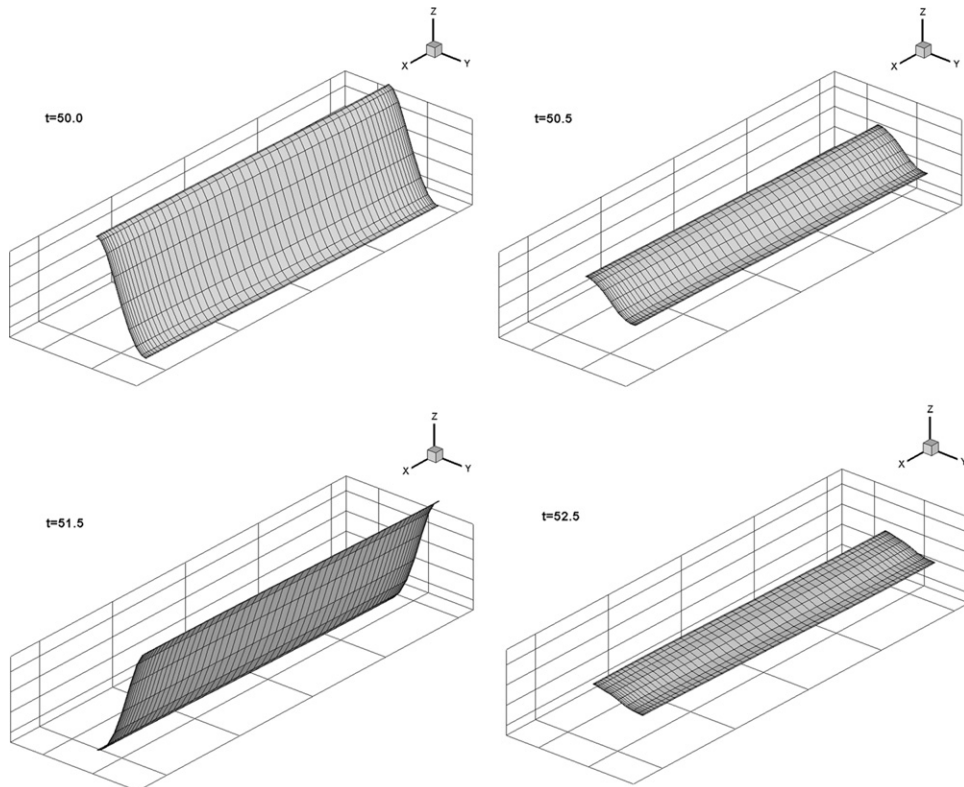

Fig. 14. Snapshots of the free surface profile: base aspect ratio=10/1, diagonal excitation, $A_x/d = A_y/d = 0.001$, $\Omega_x/\omega_{10} = 0.9999$, $\Omega_y/\omega_{01} = 0.9999$ (the profile is not scaled).

amplitude is $A_x/d=0.001$. The predicted free surface motions invariably reach stable steady state conditions, as would be expected, because of the small perturbation (A_x/d) value. All the resulting steady-state wave motions are planar, two-dimensional. Fig. 7 presents a classification of the wave patterns obtained. For $\Omega_x/\omega_{10}<0.8$, the waves are irregular and decay gradually (see Fig. 8). This regime is close to the chaotic behaviour. Beating patterns occur for $\Omega_x/\omega_{10}=0.8$ and $\Omega_x/\omega_{10}\geq1.1$ (Fig. 9). For $\Omega_x/\omega_{10}=0.8$ and $\Omega_x/\omega_{10}=1.2$, the non-dimensional period of the wave envelope is about 100 time
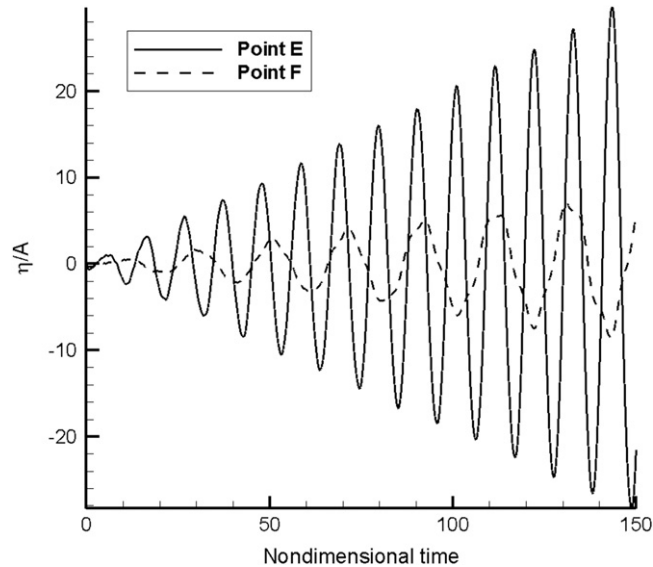

Fig. 15. Wave elevation time histories: base aspect ratio$=10/5$, diagonal excitation, $A_x/d=A_y/d=0.001$, $\Omega_x/\omega_{10}=0.9999$, $\Omega_y/\omega_{01}=0.9999$.
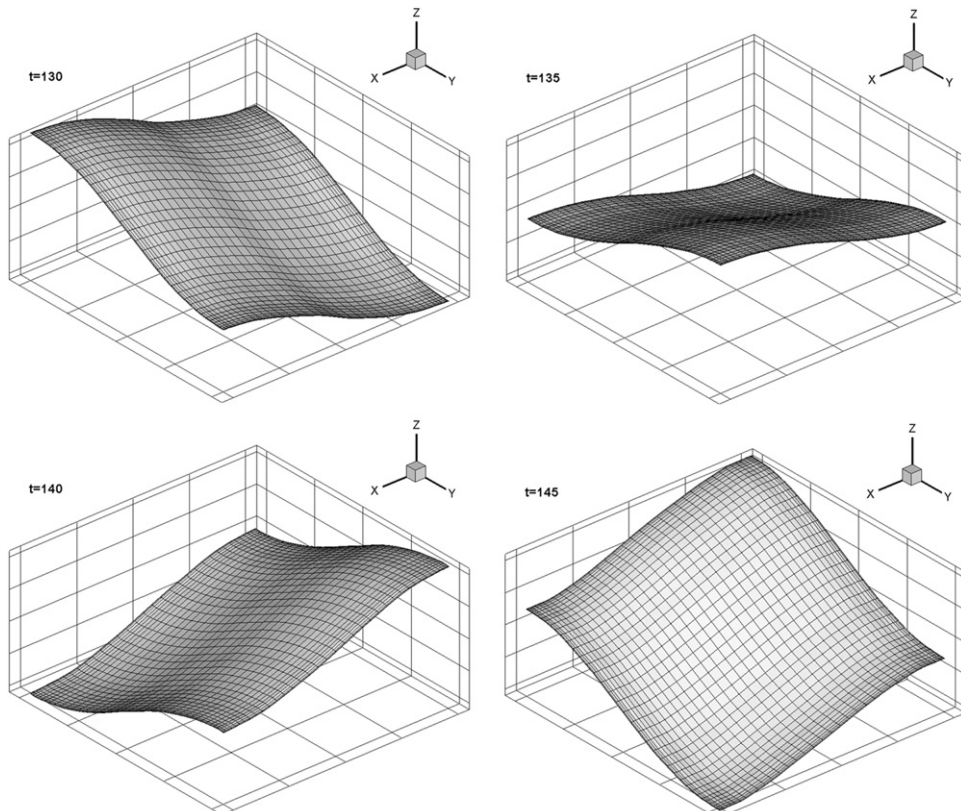

Fig. 16. Snapshots of the free surface profile: base aspect ratio$=10/9$, diagonal excitation, $A_x/d=A_y/d=0.001$, $\Omega_x/\omega_{10}=0.9999$, $\Omega_y/\omega_{01}=0.9999$ (the profile is not scaled).
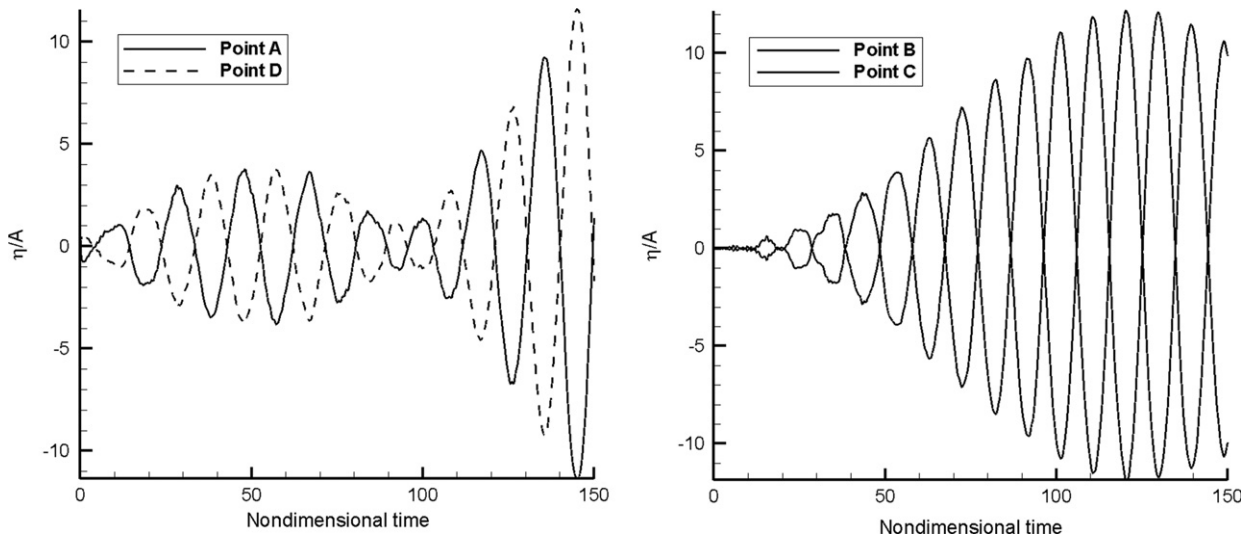
Fig. 17. Wave elevation time histories: base aspect ratio=10/9, diagonal excitation, $A_x/d=A_y/d=0.001$, $\Omega_x/\omega_{10}=0.9999$, $\Omega_y/\omega_{01}=0.9999$.
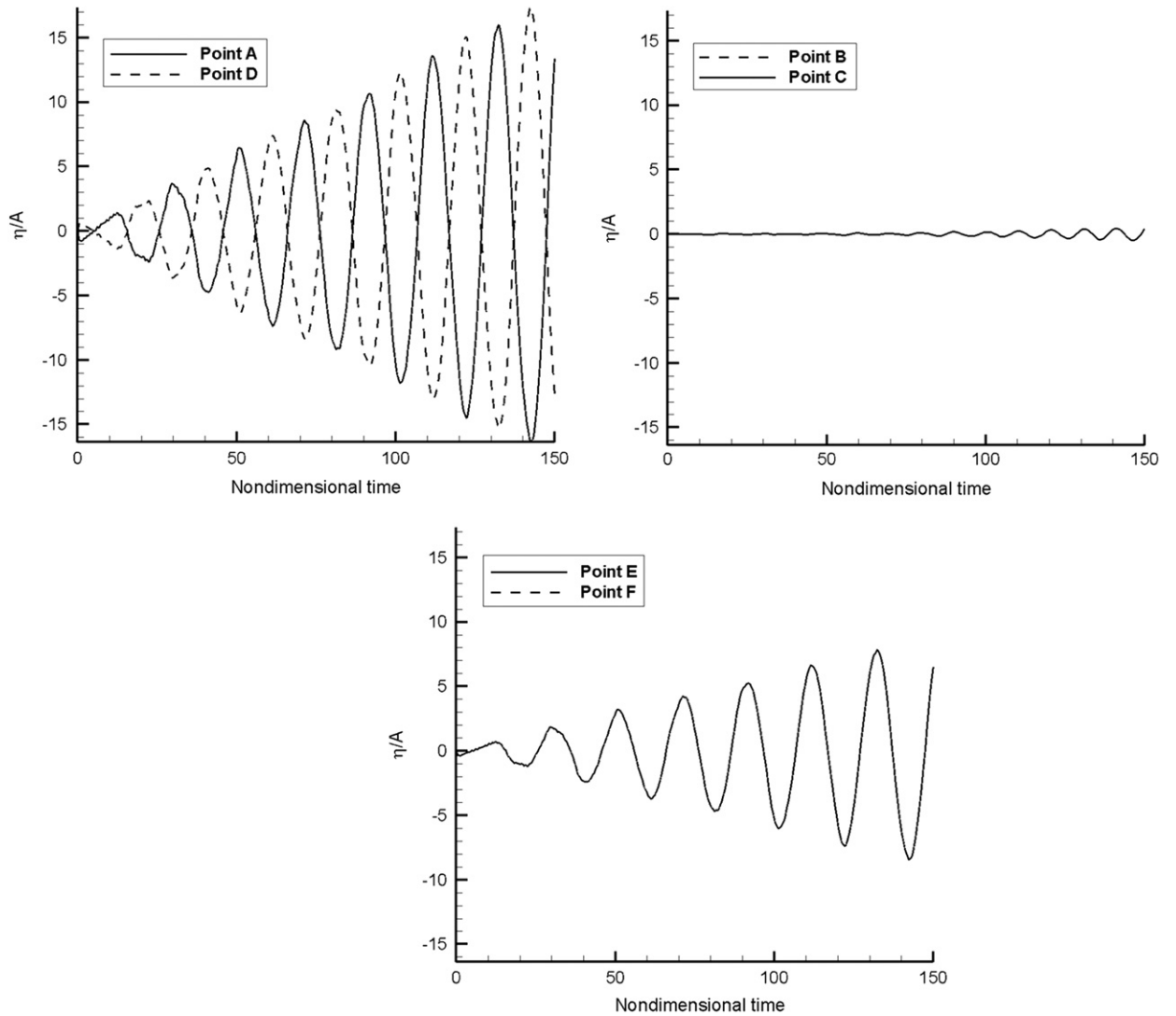

Fig. 18. Wave elevation time histories: base aspect ratio=10/10, diagonal excitation, $A_x/d=A_y/d=0.001$, $\Omega_x/\omega_{10}=0.9999$, $\Omega_y/\omega_{01}=0.9999$.

units. The maximum wave elevation for $\Omega_x/\omega_{10}=1.2$ is about 61% greater than that for $\Omega_x/\omega_{10}=0.8$, and the wave is steeper. For $\Omega_x/\omega_{10}=1.1$, the non-dimensional period of the wave envelope is more than 200 time units and the maximum wave elevation is about 84% larger than for $\Omega_x/\omega_{10}=1.2$. Fig. 10 shows the free surface time histories at frequency ratios close to resonance, in the range $0.9 \leq \Omega_x/\omega_{10} \leq 1.05$, where the wave lengths are almost the same. The maximum increasing rates of amplitude of the free surface motions are obtained for frequency ratios of 0.9999 and 1.0001.

6.2. Effect of base aspect ratio

Industrial containers usually have different base dimensions, and the length/width aspect ratio can affect the sloshing wave behaviour. Several theoretical and experimental studies have been undertaken on this topic (e.g. Feng and Sethna, 1993; Ockendon et al., 1993). Recently, Faltinsen et al. (2006) examined the nearly-square base effect on the wave regimes in a tank of intermediate water depth. In the present study, we consider four different base aspect ratios a/b in shallow water where $d/a=0.1$. The ratios are $a/b=10/1$ (very long base), 10/5 (half width base), 10/9 (nearly square base) and 10/10 (square base). Longitudinal (surge) and diagonal (surge and sway) excitations are applied separately, for two non-dimensional amplitudes $A_x/d=A_y/d=0.001$ and 0.01.

6.2.1. Resonance excitation frequency

First, we focus on surge ($\Omega_x/\omega_{10}=0.9999$) and sway ($\Omega_y/\omega_{01}=0.9999$) excitations. Fig. 11 compares wave elevation time histories for different base aspect ratios, when the excitation is longitudinal and the non-dimensional amplitude is $A_x/d=0.001$. The results demonstrate that when the basin is far from square ($a/b=10/1$ and 10/5), the sloshing rapidly evolves into standing waves at this low value of A_x/d. This phenomenon has previously been observed in certain sloshing problems, but, in such cases, the standing waves were found to take considerable time to develop and were usually driven by diagonal excitation of the tank (see Faltinsen et al., 2005). Also, there is an obvious phase shift, which is almost seiche-related behaviour (Forel, 1895). However, the standing waves exist only for certain special conditions. For example, when the excitation frequency ratio is increased to 1.1, standing waves are not found. Resonant wave motions diminish as the basin becomes less square and the base aspect ratio deviates from unity, due to asymmetric wave interactions. For
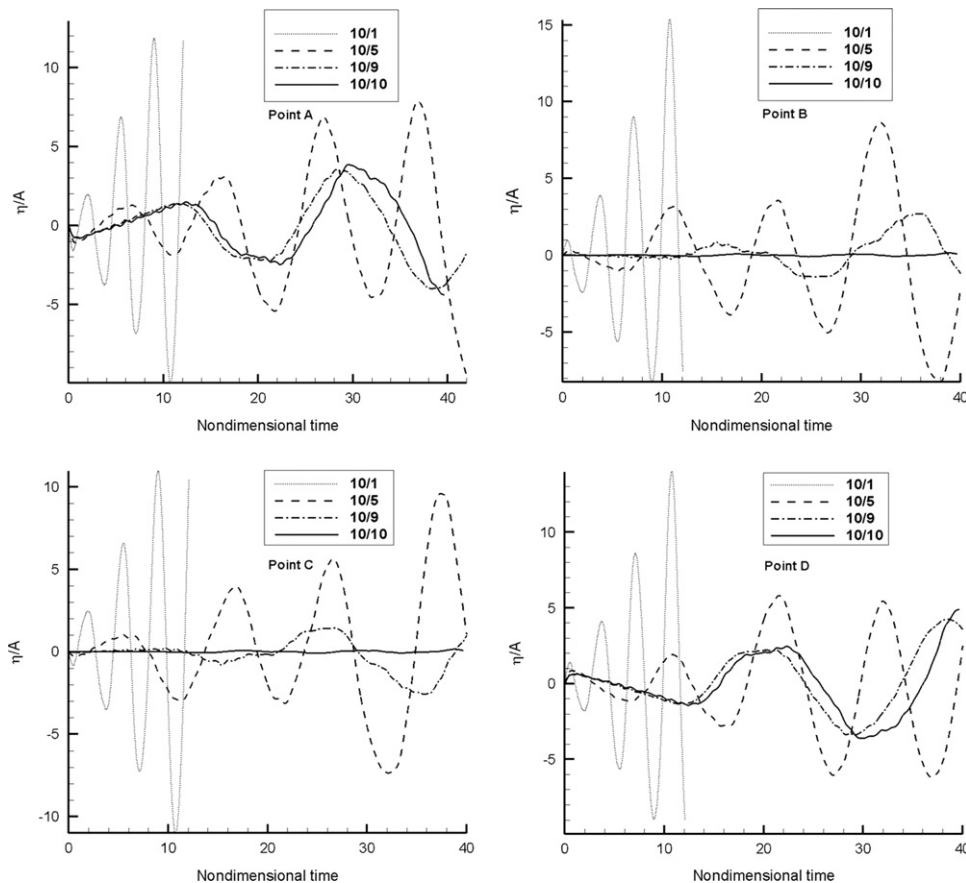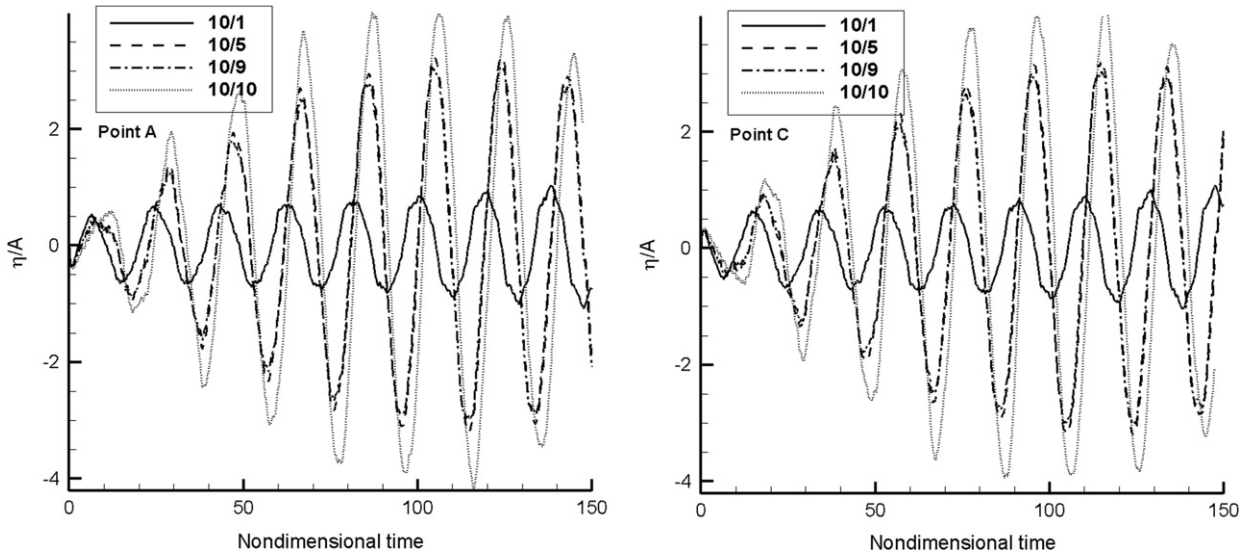

Fig. 19. Wave elevation time histories for different base aspect ratios: diagonal excitation, $A_x/d=A_y/d=0.01$, $\Omega_x/\omega_{10}=0.9999$, $\Omega_y/\omega_{01}=0.9999$.

Table 2
Effects of base aspect ratio on wave regime and pattern (resonant excitation frequency, diagonal excitation).

Base aspect ratio	Amplitude	Wave regime	Wave pattern
10/1	0.001	Planar	Resonant
10/1	0.01	Planar	Resonant
10/5	0.001	Swirling	Resonant
10/5	0.01	Swirling	Resonant
10/9	0.001	Swirling	Beating
10/9	0.01	Swirling	Beating
10/10	0.001	Diagonal	Resonant
10/10	0.01	Diagonal	Resonant

Fig. 20. Wave elevation time histories for different base aspect ratios: longitudinal excitation, $A_x/d=0.001$, $\Omega_x/\omega_{10}=1.1$.
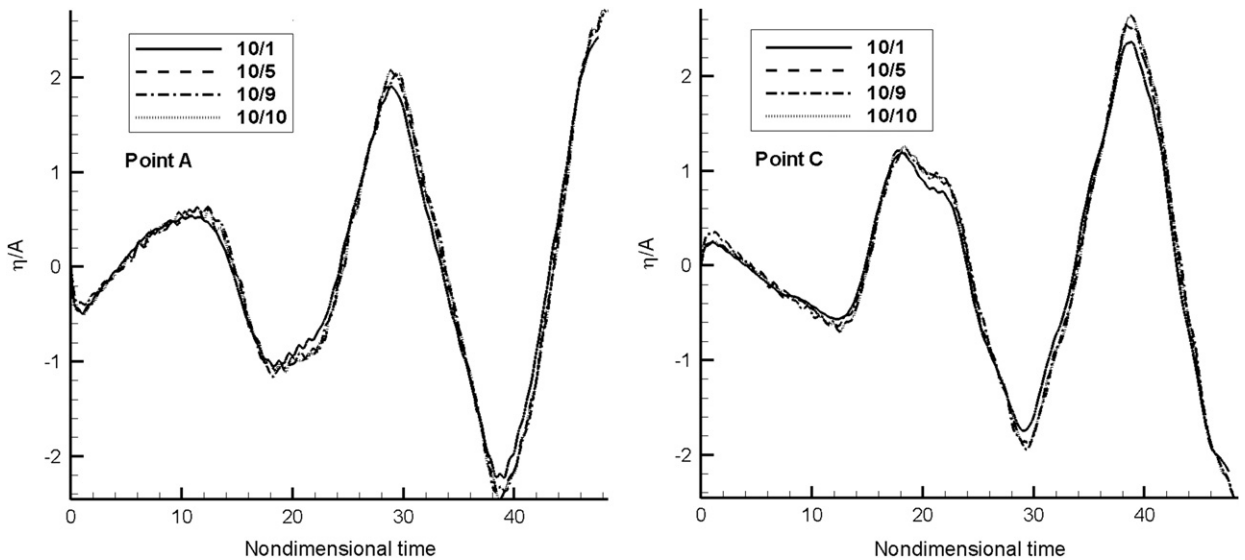
Fig. 21. Wave elevation histories for different base aspect ratios: longitudinal excitation, $A_x/d=0.01$, $\Omega_x/\omega_{10}=1.1$.

$a/b=10/9$, the maximum free surface elevation at non-dimensional time of 100 units decreases by about 47% compared with that for $a/b=10/10$. In all cases, the sloshing is planar.

Fig. 12 shows that the effect of increasing the longitudinal excitation amplitude to $A_x/d=0.01$ causes the evolution of the wave patterns to become much less sensitive to the geometric base aspect ratio of the tank.

Next, the tank is excited in two directions simultaneously, such that $A_x/d=A_y/d==0.001$. Fig. 13 depicts the free surface time histories for varying base aspect ratio. For $a/b=10/1$, the effect of sway is significantly more than surge (see Eq. (6)). In this case, when $\omega_{01}\approx540\omega_{10}$ the wave regime becomes effectively planar in the y-direction (Fig. 14). Although there are some wave perturbations in the x-direction these are unable to change the regime.

For $a/b=10/5$, the longitudinal and transverse excitation frequencies are closer, and the wave motions become swirling but with different wave elevations in the x- and y-direction (see Fig. 15 for the corresponding wave elevation time histories at points E and F). When the base aspect ratio is nearly square (such that $a/b=10/9$), swirling is preserved in the wave motion (Fig. 16), but the pattern changes to beating (Fig. 17). For $a/b=10/10$, a diagonal wave regime is established, with some perturbations induced at B and C but insufficient to change the motion (Fig. 18). Fig. 19 shows elevation time
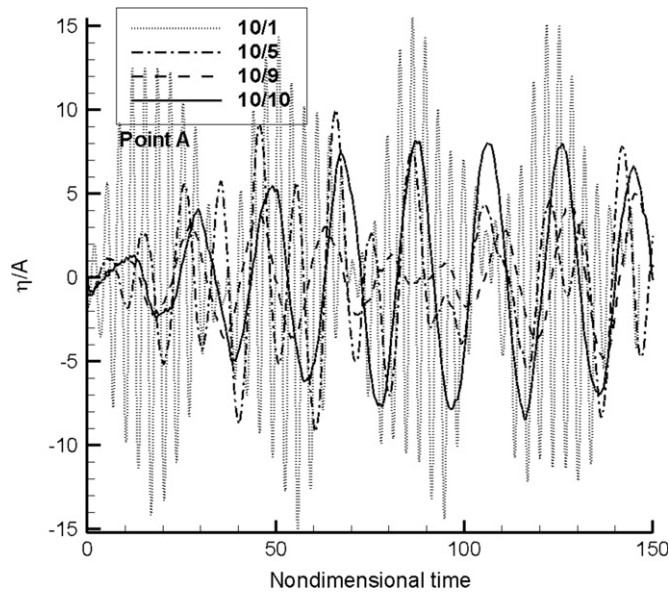

Fig. 22. Wave elevation time histories for different base aspect ratios: diagonal excitation, $A_x/d=A_y/d=0.001$, $\Omega_x/\omega_{10}=1.1$, $\Omega_y/\omega_{01}=1.1$.
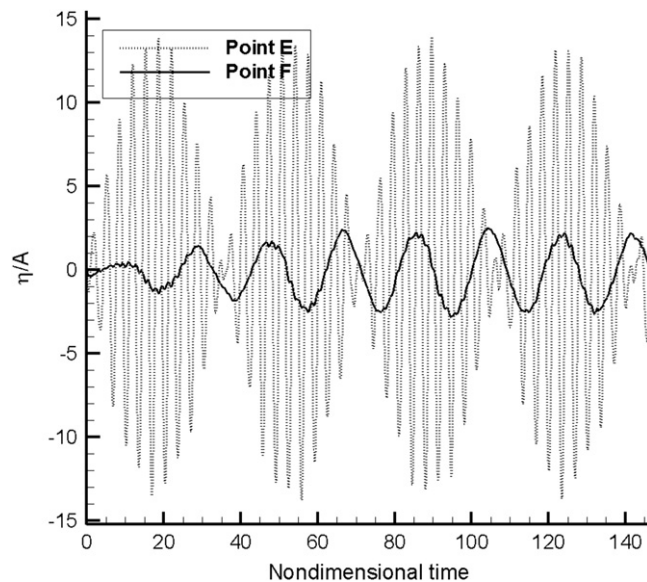

Fig. 23. Wave elevation time histories for base aspect ratio $=10/1$, diagonal excitation, $A_x/d=A_y/d=0.001$, $\Omega_x/\omega_{10}=1.1$, $\Omega_y/\omega_{01}=1.1$.

histories at A, B, C and D for $A_x/d = A_y/d = 0.01$. The wave regimes and patterns are the same as for the (almost) linear amplitude ($A_x/d = A_y/d = 0.001$) cases. Table 2 summarizes the results of the diagonal excitation tests.

6.2.2. Beating excitation frequency

Fig. 20 shows the free surface time histories at locations A and C for surge excitation at a beating frequency, $\Omega_x/\omega_{10} = 1.1$, with $A_x/d = 0.001$ for various base aspect ratios. Unlike the corresponding resonance excitation cases, standing waves do not develop for $a/b = 10/1$ and $10/5$. The envelope periods for $a/b = 10/1$ and $10/5$ are longer than for $a/b = 10/9$ and $10/10$. The regime is invariably planar, with the wave pattern exhibiting beating behaviour for all base aspect ratios. As the amplitude increases to 0.01, the wave motions become almost unaffected by the base aspect ratio (Fig. 21).

Fig. 22 depicts the free surface elevation time history for diagonal excitation of the tank with $A_x/d = A_y/d = 0.001$. For a base aspect ratio of 10/1, the primary regime of wave motion is planar in the y-direction. Fig. 23 shows the free surface motions at locations E and F. There is evidence of wave beating, for example when the free surface oscillations in the x-and y-direction almost disappear between 100 and 110 non-dimensional time units, and the wave regime becomes swirling.

As the width of the tank is increased relative to the length, the wave motions become more complicated. For $a/b = 10/5$, the wave pattern is almost beating but mixed, and includes planar, diagonal, clockwise swirling and counter-clockwise swirling regimes. Fig. 24 presents the free surface elevation time histories at locations A to F.
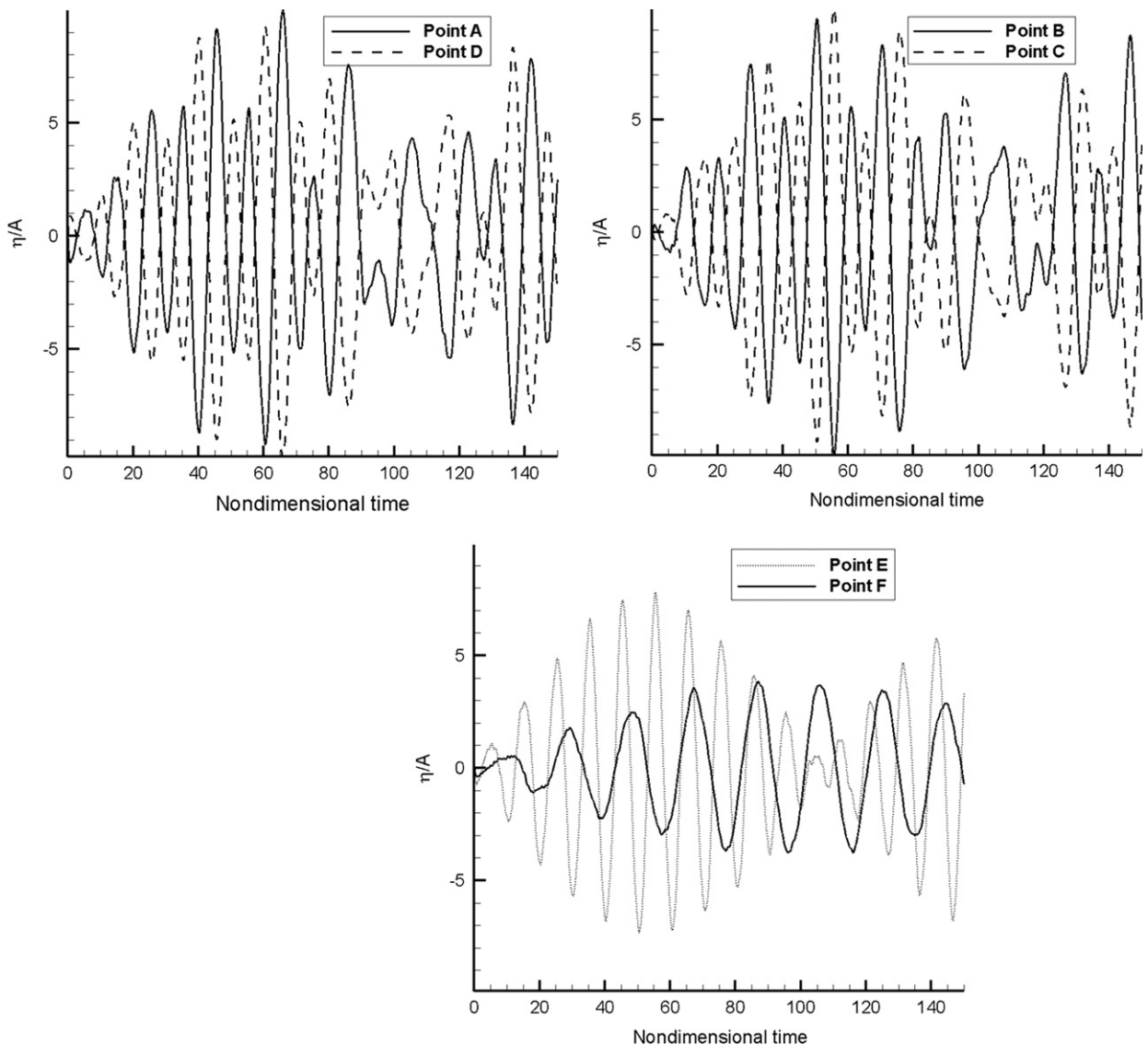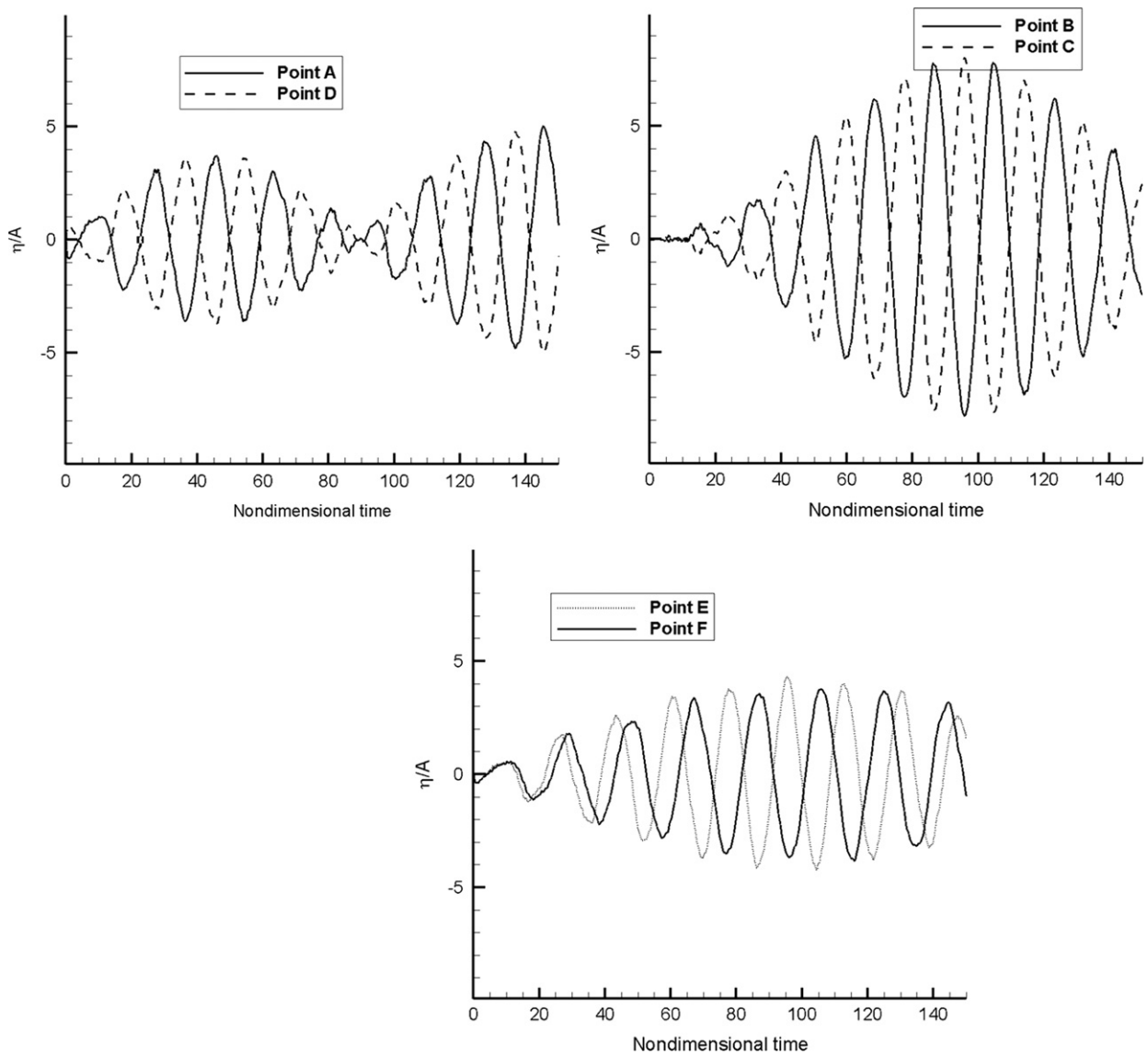

Fig. 24. Wave elevation time histories for base aspect ratio=10/5, diagonal excitation, $A_x/d = A_y/d = 0.001$, $\Omega_x/\omega_{10} = 1.1$, $\Omega_y/\omega_{01} = 1.1$.

Fig. 25. Wave elevation time histories for base aspect ratio=10/9: diagonal excitation, $A_x/d=A_y/d=0.001$, $\Omega_x/\omega_{10}=1.1$, $\Omega_y/\omega_{01}=1.1$.

When the tank has a nearly square base ($a/b=10/9$), the wave motion is swirling, although the maximum elevations at points A and D are about 60% less than points B and D. Also, the envelope durations at A and D are about 62% less than at B and C (Fig. 25). The maximum elevation is the smallest in comparison with the results obtained for other base aspect ratios. For the square base, the wave motion is diagonal and the pattern is beating, as expected. The maximum elevation in this case is between that obtained for $a/b=10/5$ and $10/9$.

The wave motion regimes and patterns obtained when the excitation amplitude is increased to $A_i/d=0.01$ are similar to those obtained for the small amplitude cases where $A_i/d=0.001$. Table 3 summarizes the results obtained for diagonal excitation. Fig. 26 compares free surface motions at the tank corners for different base aspect ratios when $\Omega_x/\omega_{10}=1.1$ and $A_i/d=0.01$.

In short, the present study shows that the base aspect ratio is very important in shallow water sloshing. More research is required, especially with regard to theory of stability and laboratory experiments.

6.3. Amplitude effect

The final part of the parameter study examines the influence of longitudinal excitation amplitude on free surface motions in a tank with dimensions $d/a=d/b=0.1$. Four different non-dimensional amplitudes are considered: $A_x/d=0.001$, 0.005, 0.01 and 0.1.

Table 3
Effect of the base aspect ratio on wave regime and pattern (beating excitation frequency, diagonal excitation).

Base aspect ratio	Amplitude	Wave regime	Wave pattern
10/1	0.001	Planar	Beating
10/1	0.01	Planar	Beating
10/5	0.001	Mixing	Beating
10/5	0.01	Mixing	Beating
10/9	0.001	Swirling	Beating
10/9	0.01	Swirling	Beating
10/10	0.001	Diagonal	Beating
10/10	0.01	Diagonal	Beating
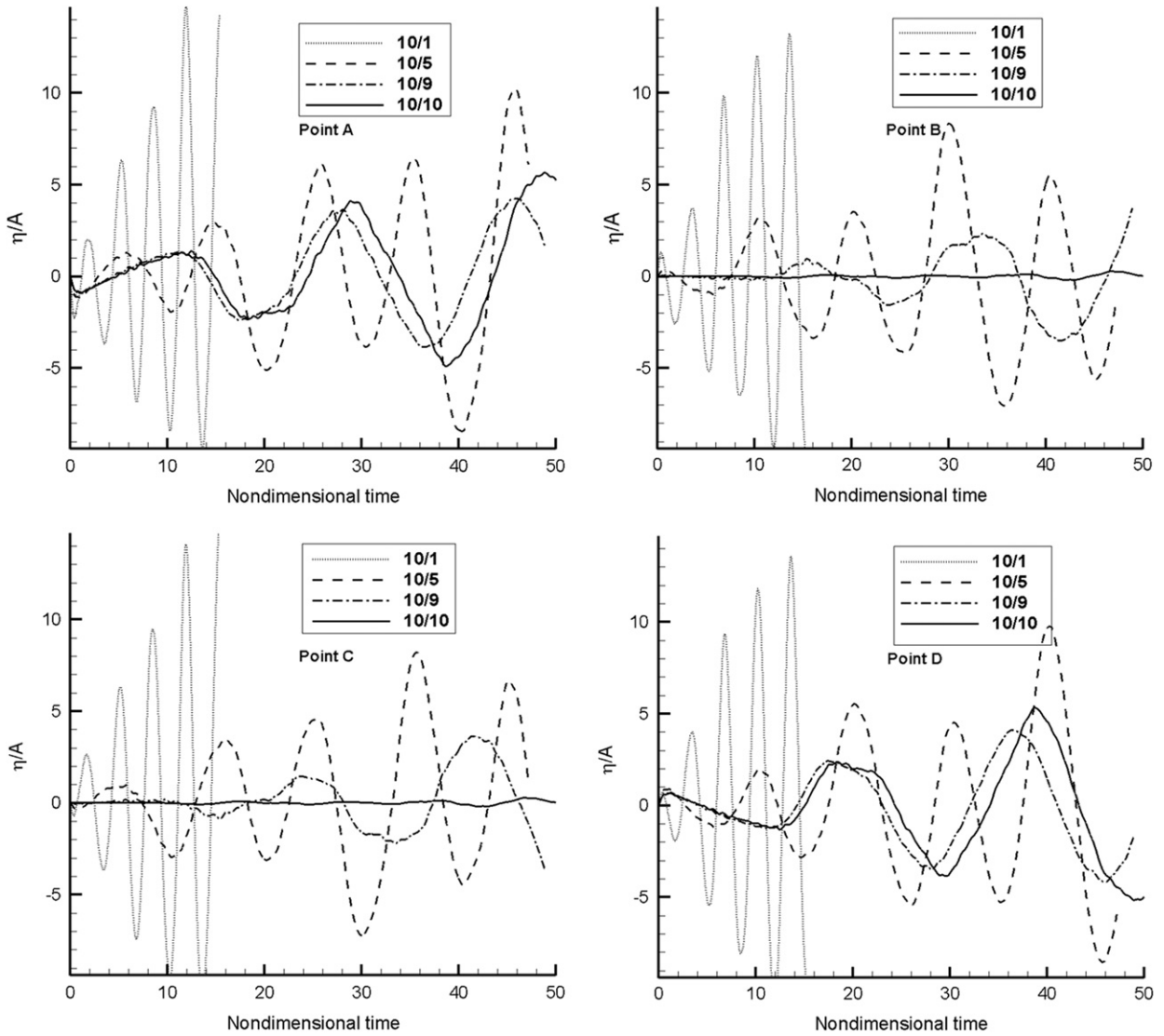
Fig. 26. Wave elevation time histories for different base aspect ratios: diagonal excitation, $A_x/d=A_y/d=0.01$, $\Omega_x/\omega_{10}=1.1$, $\Omega_y/\omega_{01}=1.1$.

Fig. 27 shows the free surface elevation time histories obtained for all four amplitudes at locations E and F when the non-dimensional excitation frequency is $\Omega_x/\omega_{10}=0.9999$. Ripples can be observed at E, and become more pronounced with excitation amplitude due to the effect of nonlinearity. At F, steep waves of growing amplitude develop with time.
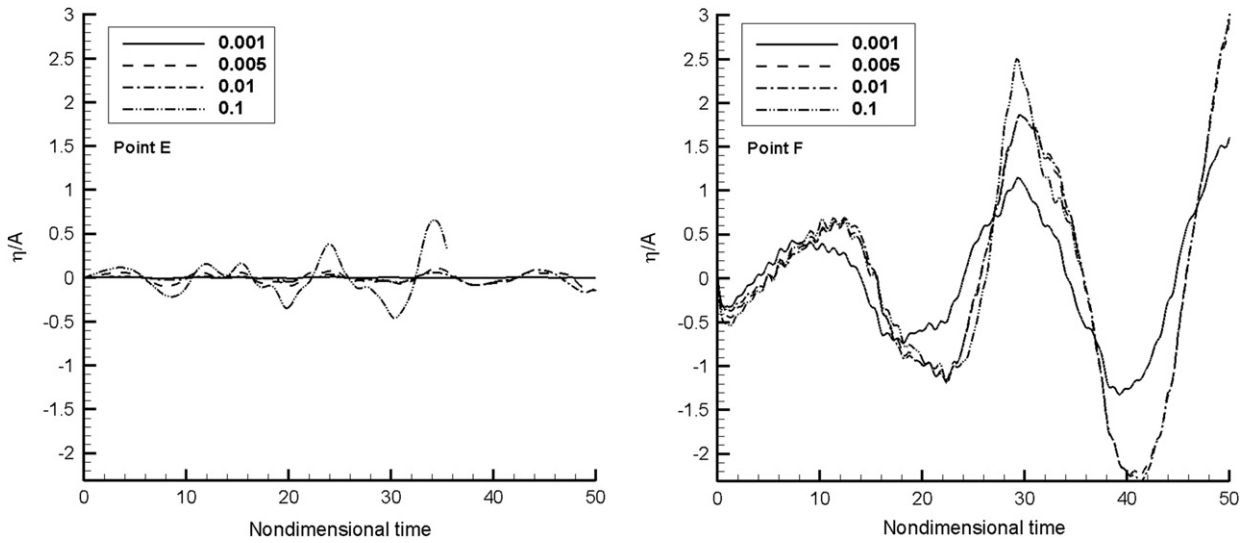
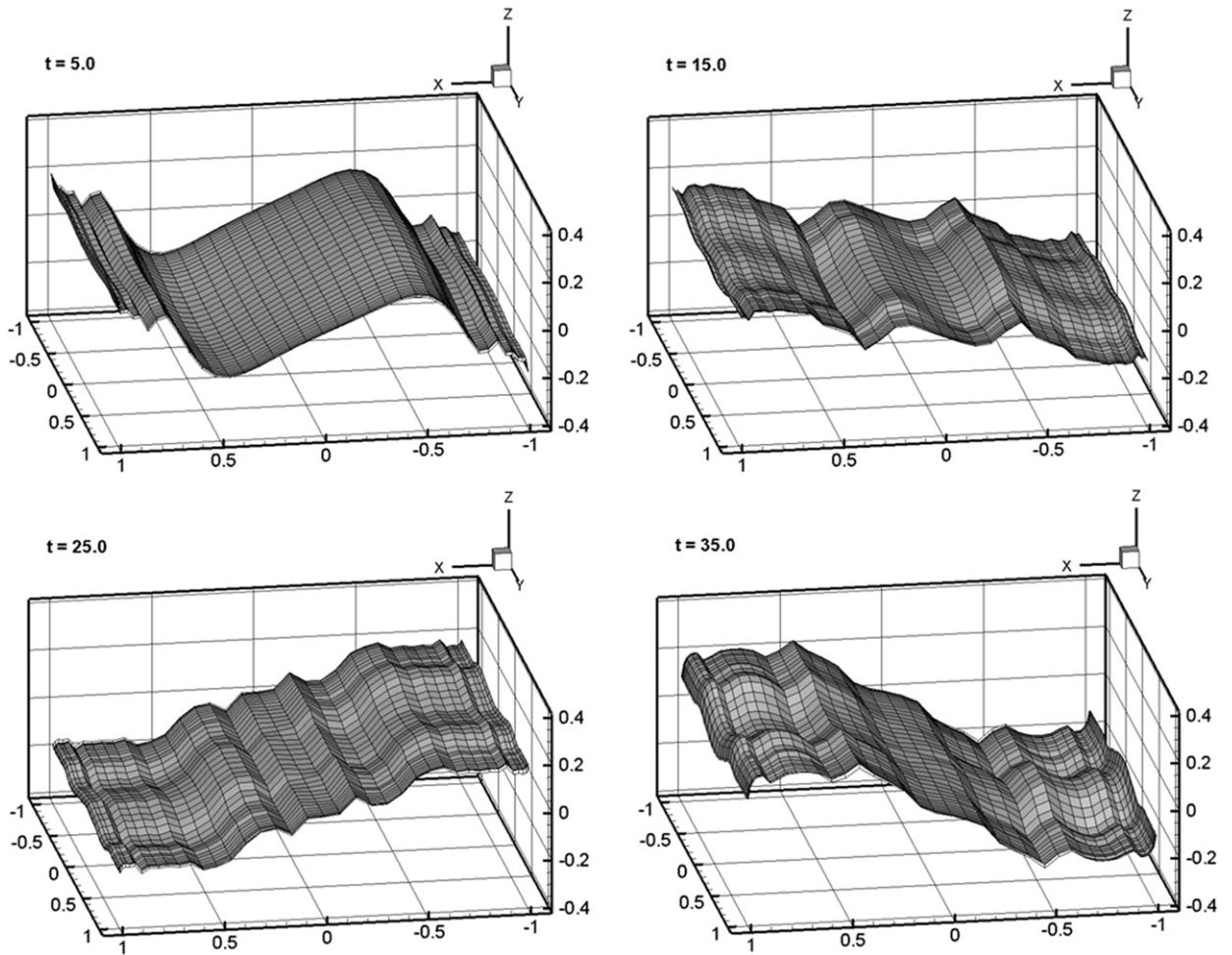**Fig. 27.** Wave elevation time histories for different excitation amplitudes, $\Omega_x/\omega_{10}=0.9999$.

Fig. 28. Snapshots of the free surface profile: $A_x/d=0.001$, $\Omega_x/\omega_{10}=0.9999$ (the profile is not scaled).
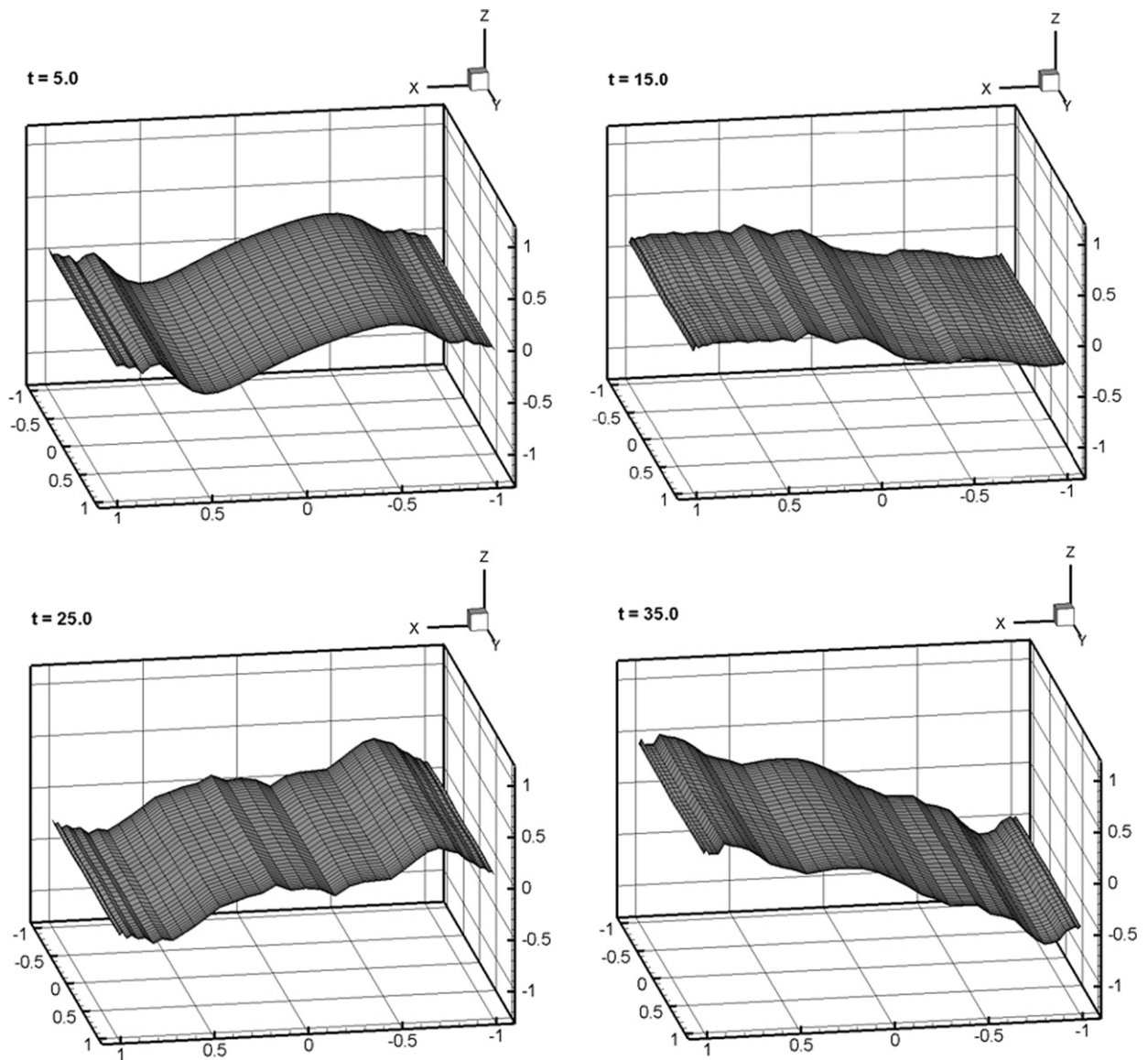
Fig. 29. Snapshots of the free surface profile: $A_x/d=0.005$, $\Omega_x/\omega_{10}=0.9999$ (the profile is not scaled).

Wave motions are planar in all cases. Figs. 28–31 show free surface snapshots of all cases when non-dimensional times are equal to 5, 15, 25 and 35. When $A_x/d=0.001$ (Fig. 28), the sloshing elevation is lower than other cases. Some perturbations are seen but they cannot change the wave regime. When $A_x/d=0.005$ and 0.01 (Figs. 29 and 30), perturbations are much less than the first case. In the largest amplitude case ($A_x/d=0.1$), the wave behaviour is almost the same as the other cases before 30.0 non-dimensional time units. But after that the bore appears gradually. This behaviour can be seen obviously in the last snapshot of the Fig. 31. Similar effects are noted by Armenio and La Rocca (1996) for two-dimensional roll motion of water in a tank.

Fig. 32 shows the free surface time histories obtained for $\Omega_x/\omega_{10}=1.1$. The results are essentially the same as for $\Omega_x/\omega_{10}=0.9999$, except that the bore is not created until the end of the simulation.

7. Conclusions

A pseudospectral σ-transformation model has been developed for simulating sloshing waves in a 3-D rectangular tank. The model was verified against analytical solutions for sloshing in a two-dimensional tank and an alternative numerical prediction for a three-dimensional tank. A parameter study was undertaken for sloshing in a shallow water tank, where $d/a=0.1$ and the excitation frequency, base aspect ratio, and excitation amplitude were varied. First, the wave pattern was
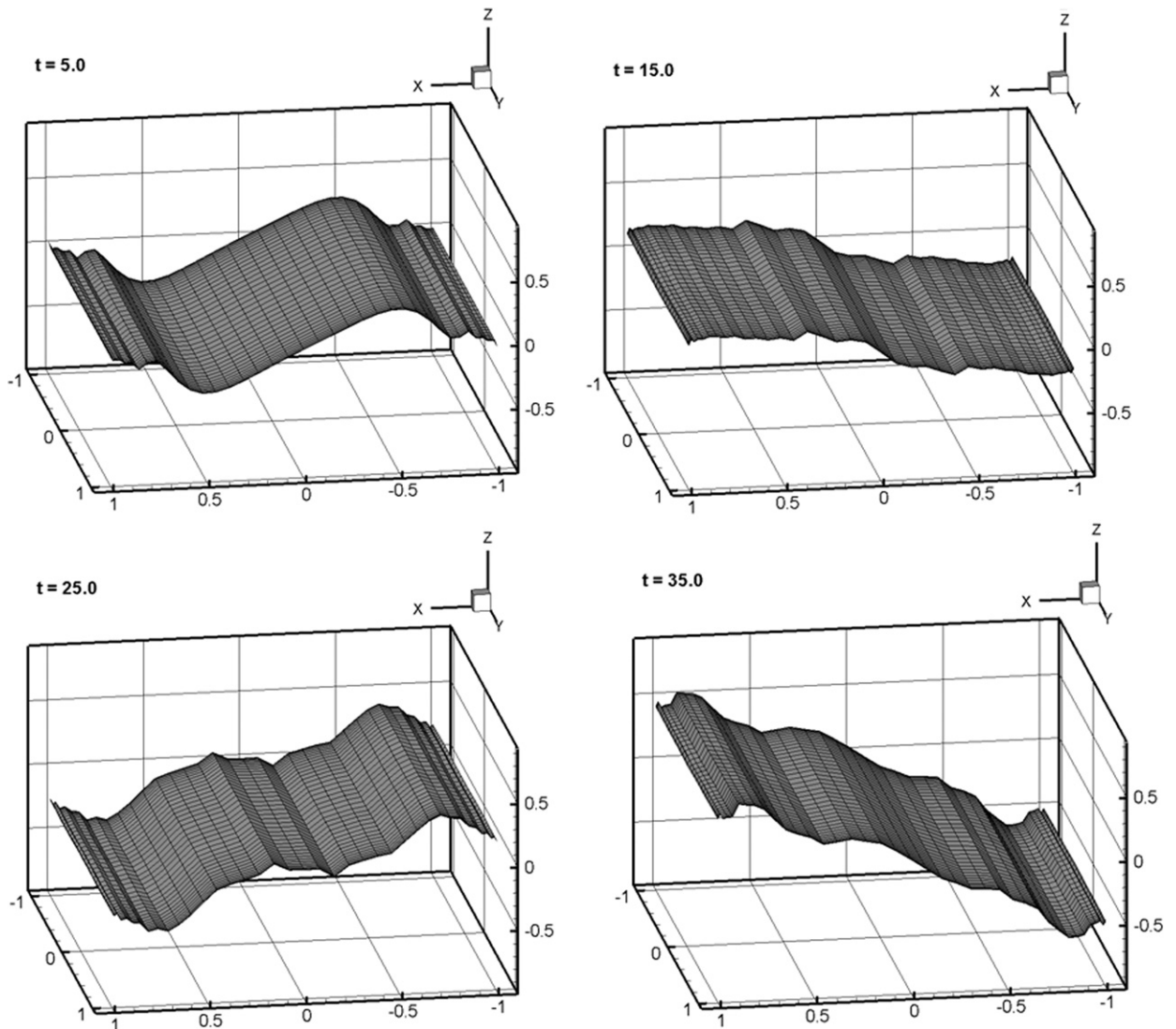
Fig. 30. Snapshots of the free surface profile: $A_x/d=0.01$, $\Omega_x/\omega_{10}=0.9999$ (the profile is not scaled).

classified for small amplitude longitudinal excitation of $A_x/d=0.001$ in a square tank for various near-resonant excitation frequencies. It was found that the patterns altered from decay, to beating, to resonant, to beating as Ω_x/ω_{10} varied from 0.6 to 1.2.

The sloshing dynamics obtained for four base aspect ratios was studied. For small-amplitude longitudinal resonance excitation, the wave pattern was that of standing waves when the base aspect ratio is far from unity. In contrast, resonant waves were produced in nearly square and square basins. For the largest amplitude longitudinal excitation ($A_x/d=A_y/d=0.01$) the resonant free surface motions were similar regardless of the base aspect ratio, with the wave height increasing monotonically. The wave pattern and wave regime were more sensitive to the base aspect ratio of the tank when the resonant excitation was diagonal. Table 2 summarizes the findings for the resonant excitation cases. For a beating excitation frequency in the longitudinal direction, the wave motions were in the planar regime with a beating pattern, as expected, regardless of base aspect ratio. For diagonal beating excitation, the wave regimes were dependent on the base aspect ratio. Table 3 summarizes the findings for the beating excitation cases. Finally, the effect of longitudinal excitation amplitude was considered. For large amplitude resonance excitation, a bore was induced in the tank. In general, the larger was the amplitude, the steeper the waves due to the effect of nonlinearity.

The present study has demonstrated the capability of the PSME method to simulate the behaviour of sloshing waves in a tank. Also, results show that in shallow water containers, the behaviour of the sloshing strongly depends on the base aspect ratio. It is more obvious when the exciting amplitude is small. Future investigation is required into the effect of base aspect ratio on sloshing in shallow and very shallow water containers.
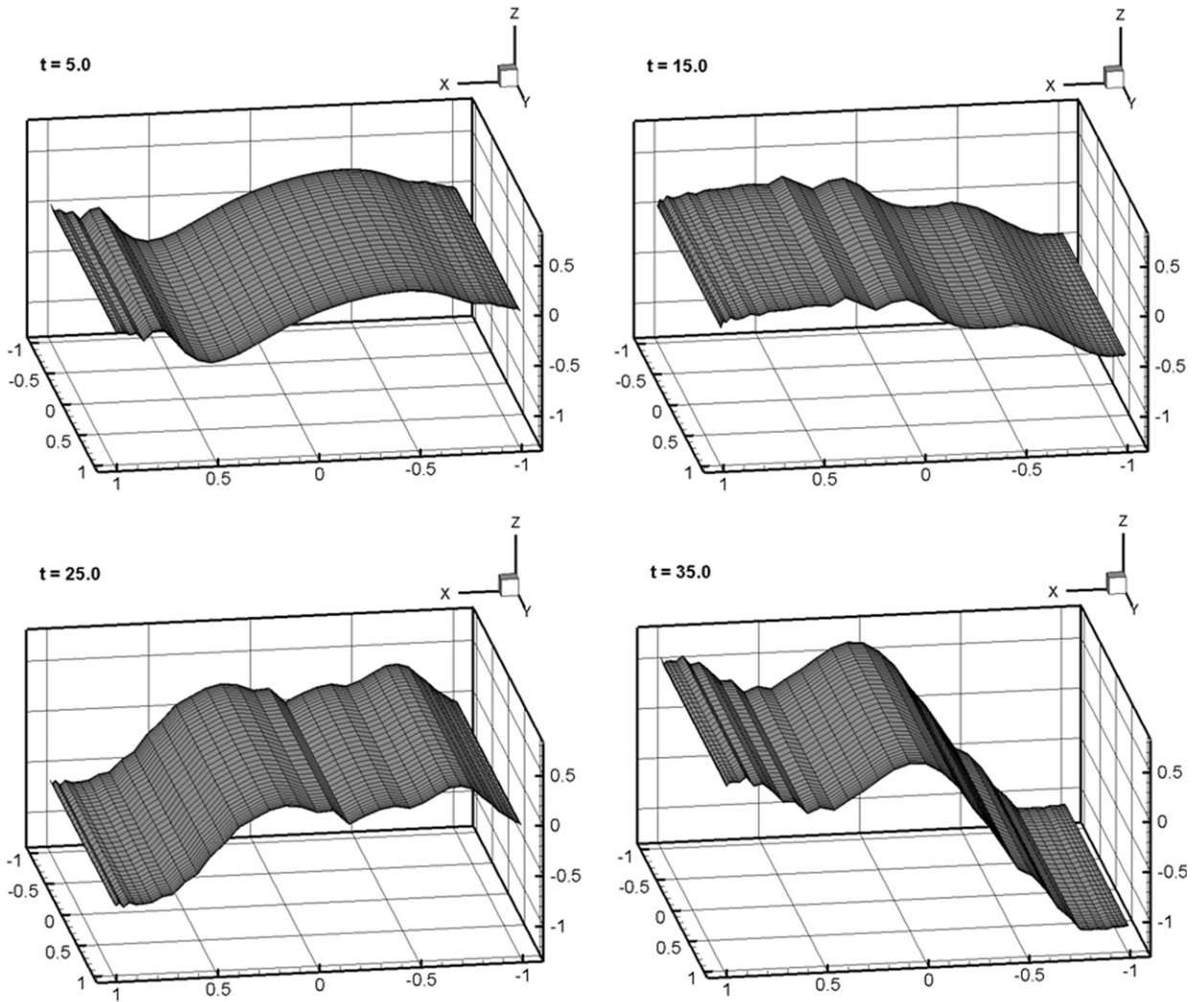
Fig. 31. Snapshots of the free surface profile: $A_x/d=0.1$, $\Omega_x/\omega_{10}=0.9999$ (the profile is not scaled).
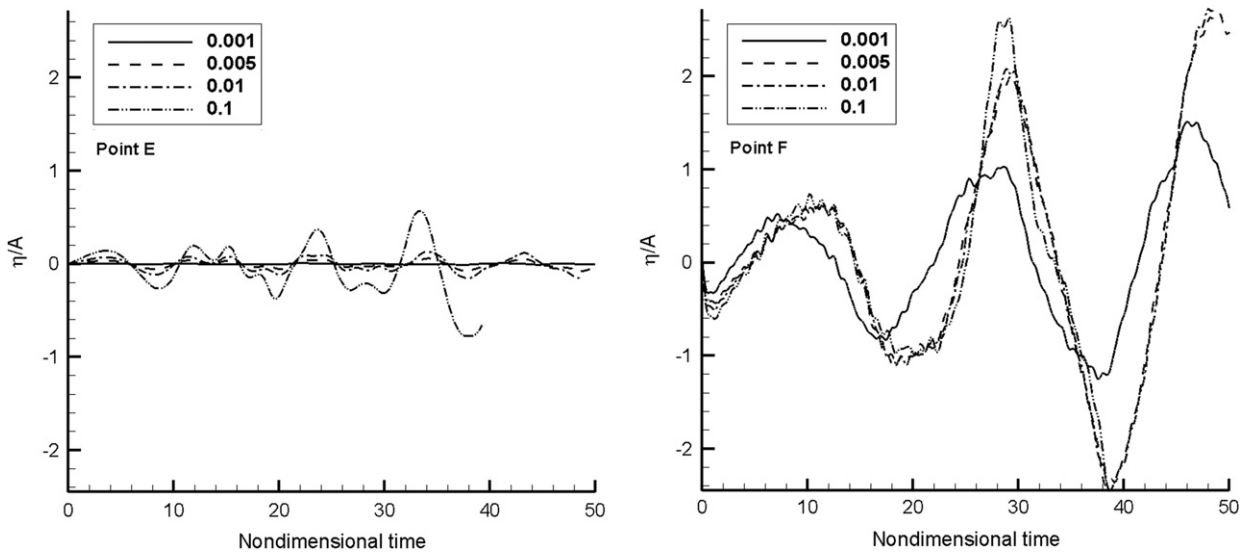

Fig. 32. Wave elevation time histories for different longitudinal excitation amplitudes, at $\Omega_x/\omega_{10}=1.1$.

Acknowledgements

References

Abramson, H.N., 1966. The Dynamics of Liquids in Moving Containers. Report sp 106, NASA.

Akyildiz, H., Erdem Unal, N., 1996. Sloshing in a three-dimensional rectangular tank: numerical simulation and experimental validation. Ocean Engineering 33, 2135–2149.

Alemi Ardakani, H., Bridges, T.J., 2011. Shallow-water sloshing in vessels undergoing prescribed rigid-body motion in three dimensions. Journal of Fluid Mechanics 667, 474–519.

Armenio, V., La Rocca, M., 1996. On the analysis of sloshing of water in rectangular containers: numerical study and experimental validation. Ocean Engineering 23, 705–739.

Chen, W., Haroun, M.A., Liu, F., 1996. Large amplitude liquid sloshing in seismically excited tanks. Earthquake Engineering & Structural Dynamics 25, 653–669.

Chern, M.J., Borthwick, A.G.L., Eatock Taylor, R., 1999. A pseudospectral σ-transformation model of 2D nonlinear waves. Journal of Fluids and Structures 13, 607–630.

Chern, M.J., Borthwick, A.G.L., Eatock Taylor, R., 2001. Simulation of nonlinear free surface motions in a cylindrical domain using a Chebyshev Fourier spectral collocation method. International Journal of Numerical Methods in Fluids 36, 465–496.

Curadelli, O., Ambrosini, D., Mirasso, A., Amani, M., 2010. Resonant frequencies in an elevated spherical container partially filled with water: FEM and measurement. Journal of Fluids and Structures 26, 148–159.

El-Sayad, M.A., Hanna, S.N., Ibrahim, R.A., 1999. Parametric excitation of nonlinear elastic systems sloshing impact. Nonlinear Dynamics 18, 25–50.

Faltinsen, O.M., 1978. A numerical nonlinear method of sloshing in tanks with two-dimensional flow. Journal of Ship Research 22, 193–202.

Faltinsen, O.M., Timokha, A.N., 2001. Asymptotic modal approximation of nonlinear resonant sloshing in a rectangular tank with small fluid depth. Journal of Fluid Mechanics 470, 319–357.

Faltinsen, O.M., Rognebakke, O.F., Timokha, A.N., 2003. Resonant three-dimensional nonlinear sloshing in a square-base basin. Journal of Fluid Mechanics 487, 1–42.

Faltinsen, O.M., Rognebakke, O.F., Timokha, A.N., 2005. Classification of three-dimensional nonlinear sloshing in a square-base tank with finite depth. Journal of Fluids and Structures 20, 81–103.

Faltinsen, O.M., Rognebakke, O.F., Timokha, A.N., 2006. Resonant three-dimensional nonlinear sloshing in a square-base basin. Part 3: base aspect ratio perturbations. Journal of Fluid Mechanics 551, 93–116.

Faltinsen, O.M., Timokha, A.N., 2009. Sloshing. Cambridge University Press, Cambridge.

Feng, Z.C., Sethna, P.R., 1993. Symmetry-breaking bifurcations in resonant surface waves. Journal of Fluid Mechanics 199, 495–518.

Forel, F.A., 1895. Le Leman: Monographie Limnologique. Rouge, Lausanne.

Frandsen, J.B., 2004. Sloshing motion in excited tank. Journal of Computational Physics 196, 53–87.

Huang, Z.J., Hsiung, C.C., 1996. Nonlinear shallow-water flow on deck. Journal of Ship Research 40, 303–315.

Hussaini, M.Y., Zang, T.A., 1987. Spectral methods in fluid dynamics. Annual Review of Fluid Mechanics 19, 339–367.

Hutton, R.E., 1962. An Investigation of Resonance, Nonlinear and Nonplanar Free Surface Oscillations of Fluid. Ph.D. Thesis, UCLA.

Ibrahim, R.A., Pilipchuck, V.N., Ikeda, T., 2001. Recent advances in liquid sloshing dynamics. Applied Mechanics Review 54, 133–199.

Ibrahim, R.A., 2005. Liquid Sloshing Dynamics. Cambridge University Press, Cambridge.

Ku, H.C., Hatziavramidis, D., 1985. Solutions of the 2-dimensional Navier–Stokes equations by Chebyshev expansion methods. Computers & Fluids 13, 99–113.

Moiseyev, N.N., 1958. On the theory of nonlinear vibration of a liquid of finite volume. Applied Mathematics and Mechanics 22, 612–621.

Ockendon, H., Ockendon, J.R., Peake, M.R., Chester, W., 1993. Geometrical effects in resonant gas oscillations. Journal of Fluid Mechanics 257, 201–217.

Okamoto, T., Kawahara, M., 1990. Two-dimensional sloshing analysis by Lagragian finite element method. International Journal of Numerical Methods in Fluids 11, 453–477.

Penny, W.G., Price, A.T., 1952. Finite periodic stationary waves in a perfect liquid—Part II. Philosophical Transactions of the Royal Society A, 254–284.

Stoker, J.J., 1957. Water waves. Interscience Publishers Inc., New York.

Sun, L., Eatock Taylor, R., Taylor, P.H., 2010. First- and second-analysis of resonant waves between adjacent barges. Journal of Fluids and Structures 26, 954–978.

Wu, C.H., Chen, B.F., 2009. Sloshing waves and resonance modes of fluid in a 3-D tank by a time-independent finite difference method. Ocean Engineering 36, 500–510.

Wu, G.X., Ma, Q.W., Eatock Taylor, R., 1998. Numerical simulation of sloshing waves in a 3-D tank based on a finite element methods. Applied Ocean Research 20, 337–355.